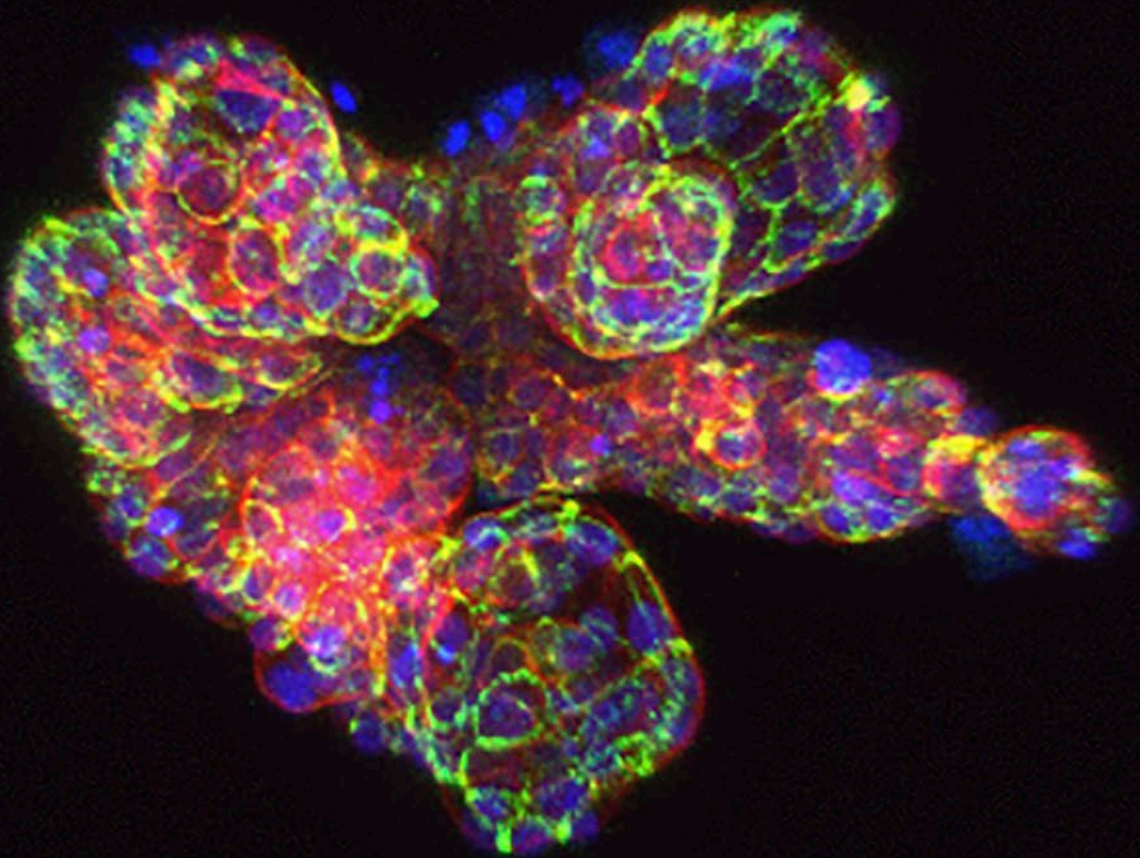


Looking Deeper Imaging and Analysis of Advanced 3D Cellular Models



Looking Deeper

Imaging and Analysis of Advanced 3D Cellular Models

01 Smarter Cell Culture

Optimizing stem cell differentiation

Observing Differentiation into iPS Cell-Derived Liver Organoids	4
Variations in the Efficiency of Liver Organoid Differentiation among iPS Cell Lines	5

02 Capturing Complexity

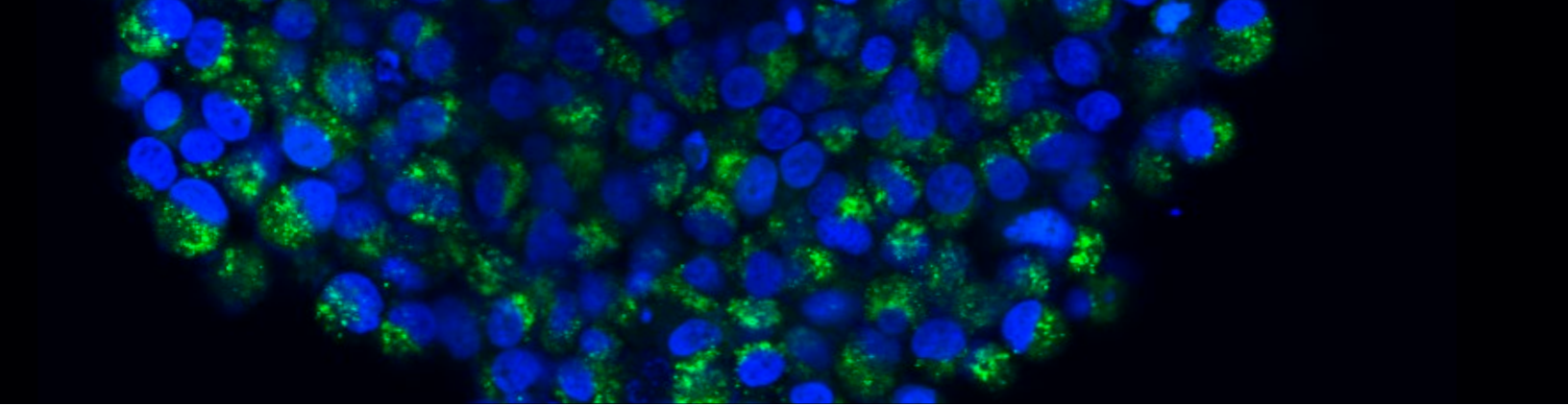
Breakthroughs in organoid imaging

Breakthrough in Live Cell Microscopy of 3D Cellular Models	11
An In Vitro System for Evaluating Molecular Targeted Drugs Using Lung Patient-Derived Tumor Organoids	18

03 Perceiving Cellular Processes

Analyzing diverse data from 3D cellular models

3D Analysis of Patient-Derived Tumor Organoids	37
Evaluation of Drug Efficacy—The Response of Spheroids to a Drug	42
Fluorescent Image Analysis—3D Spheroid Invasion in a Collagen Gel	43
True 3D Analysis of an Intracellular Autophagic Pathway in a 3D Spheroid Model	44



Introduction

With multiple advantages over conventional two-dimensional (2D) models, three-dimensional (3D) cellular models are expanding our understanding of complex biological systems and providing scientists with unique insights in areas ranging from drug discovery to cancer research.

By accurately recreating characteristics such as cell-cell and cell-matrix interactions, 3D cell models such as spheroids and organoids provide more physiologically relevant experimental models with the potential to be rapidly translated into therapeutic applications. For example, 3D cellular models are more predicative of in vivo responses during high-throughput compound testing, making them key to the development of personalized medicine. 3D cellular models can also enhance research into other cellular processes, such as proliferation, differentiation, and migration, as well as generate more reliable data on gene and protein expression.

With the number and complexity of 3D cellular models growing every year, keeping up to date with these advances is crucial for scientists in a range of research areas. In this e-book, we highlight examples of some of the most important 3D cellular models and explore how design features of the latest cell culture and imaging equipment are helping scientists realize the astounding potential of 3D cellular models.

Using 3D cell culture techniques, human induced pluripotent stem (iPS) cell lines can be differentiated into organoids—powerful disease models used in the development of new diagnostics, drug discovery, and in research into disease progression or embryonic development. In the first chapter of this e-book, we shed light on the process of iPS cell differentiation and discuss how the OLYMPUS Provi™ CM20 incubation monitoring system provides scientists with a powerful tool for quality control and data management during differentiation experiments.

With more physiological cellular morphology and functionality, patient-derived 3D cellular models such as spheroids or organoids make ideal models for compound profiling—taking us one step closer to truly personalized medicine. In the second chapter of our e-book, we explore how patient-derived tumor organoids are used to evaluate the effect of molecular targeted drugs and learn how the deep-tissue imaging capabilities of the FV3000 confocal laser scanning microscope enable analysis of organoids with a wide range of structural features. We also give a useful insight into the advantages of multiphoton microscopy over other 3D imaging platforms, providing tips and tricks on how to maximize the quality of 3D cellular images gained with the FVMPE-RS multiphoton microscope.

Making sense of the complex data generated from 3D cellular models requires not only powerful microscope systems, but also advanced methods of analysis. In the final chapter, we discover how features of NoviSight™ analysis software enable scientists to accurately measure cancer spheroid morphology, rapidly assess the live/dead status of cells upon drug treatment, and quantify invasion of complex-shaped cancer spheroids.

Comparing Human iPS Cell Lines Using the CM20 Incubation Monitoring System

Observing Differentiation into iPS Cell-Derived Liver Organoids

Introduction

Induced pluripotent stem (iPS) cells are widely used for basic research on embryology, such as cell differentiation and organ formation, as well as drug discovery research and developing diagnostic methods for diseases. To date, many iPS cell lines have been established globally, but their properties—such as differentiation potential and growth speed—differ among the strains. While these differences are known, they have never been quantified using cells grown under the same environmental conditions. This makes it difficult to determine whether these variations are due to differences in environment and procedures between labs or whether they are inherent in the cell lines themselves. Even if there are variations in the properties of differentiated cells derived from iPS cells, they are not discovered until the culture is completed, so cells that have been induced to differentiate may have abnormalities. Against this background, having a tool that enables long-term iPS cell monitoring and efficient quality control and data management of the process up to the differentiation induction experiment is important.

Quantitative Cell Culture Data Analysis Using the CM20 Incubation Monitoring System

In this study, 12 human iPS cell strains established from different donors were cultured in the same process, and data on the growth process of each cell line were obtained using the Olympus CM20 incubation monitoring system.

Culture protocol

Maintenance of the human iPS cell cultures was performed in a 6-well plate under feeder-free conditions using StemFit AK02N medium (Ajinomoto Co., Inc.) and iMarix-511 (Matrixome Inc.) plate-coating matrix. They were subcultured using unicellularizing with a detachable Accutase solution with seeding at $1.0\text{--}2.0 \times 10^4$ cells/ well, and cultured in StemFit AK02N medium supplemented with Y-27632 for 24 hours. After, the human iPS cells were proliferated by exchanging with StemFit AK02N medium with no Y-27632 and then cultured for about 1 week while exchanging the medium once every two days (Fig . 1).

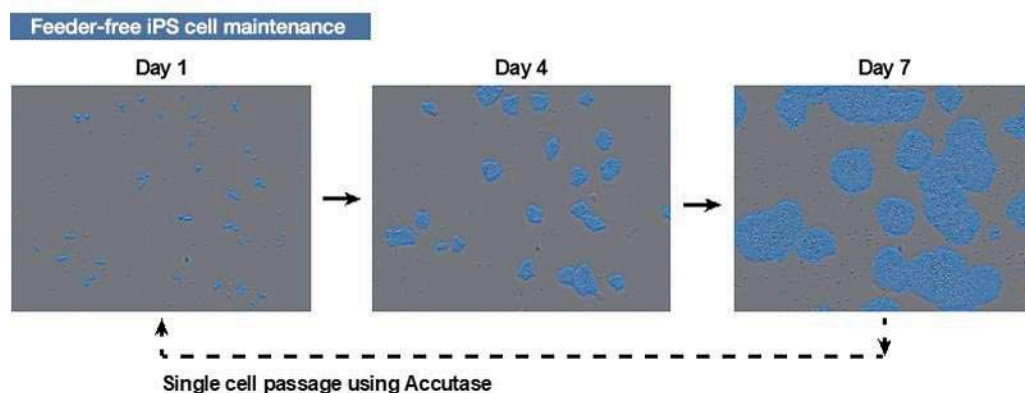


Figure 1. How human iPS cells are cultured

Comparing Human iPS Cell Lines using the CM20 Incubation Monitoring System

Variations in the Efficiency of Liver Organoid Differentiation among iPS Cell Lines

Introduction

The technology of constructing human iPS cell-derived mini-tissues/organs—called organoids—has rapidly progressed to the point that three-dimensional tissues can be utilized as an avatar of human organs. Many iPS cell lines established both from healthy subjects and patients worldwide can be utilized for organoid studies, which aim to clarify the genomic background of diseases and the predisposition to diseases for each patient by evaluating the functional and individual differences of the generated organoids. However, the process of generating organoids of the target organs generally requires more than one month and is expensive. The stability and reproducibility of organoid generation still remains a major challenge due to the variability in differentiation ability and proliferation rate among the iPS cell lines used. This is one of the barriers to the development of organoid research based on the comparison of multiple samples derived from different iPS cells.

In a previous study (1), we quantitatively monitored iPS cells over a long period of time to better dissect differences in the undifferentiated state and their relationship to cell line-dependent variation in organoid differentiation.

Among human iPS cell lines derived from 12 donors, certain lines often failed to differentiate into liver organoids in spite of the same differentiation protocol applied across all cell lines tested. In this study, we conducted an experiment to better understand the relationship of iPS cell lines between the properties at undifferentiated states before differentiation induction and differentiation potential into liver organoids.

Using iPS Cell-Monitoring Data from the CM20 System to Evaluate Organoid Differentiation

Olympus' CM20 incubation monitoring system enabled us to quantitatively measure the culture status and acquire measurement data that could easily be compared to past results. The iPS cell colony number and density data can be easily exported to a CSV file for more detailed analysis.

In this study, we monitored the growth of human iPS cell lines from 12 donors during their maintenance, and then exported time-dependent colony number and density data for each cell line. We then applied the differentiation protocol that we recently developed (2) to obtain liver organoids. After about one month, we counted the number of generated organoids and measured the level of albumin secretion as a function of the liver organoid. We also compared the iPS cell growth data obtained before differentiation with the data of their corresponding liver organoids for each cell line.



CM20 Monitoring System Benefits

The CM20 cell incubation monitoring system delivers quantitative data remotely for accurate and consistent results throughout your lab. Place your cell culture vessel on the imaging head inside the incubator. The system will periodically scan it, count the cells, and measure confluency. Data and images are wirelessly communicated from your computer workstation so that you can monitor progress without removing cultures from the incubator. When criteria are met, the system will alert you that cells are ready for passage.

- 1 Label-free, quantitative results
- 2 Reproducible, comparable data
- 3 Easy-to-use system

Culture Protocol and Data Analysis

Twelve human iPS cell lines were maintained in a 6-well plate under feeder-free conditions. Approximately one week after passage, the cells were dissociated into single cells with Accutase and then seeded on a new plate. They were stimulated with Activin A and BMP4 to differentiate from undifferentiated states into definitive endoderms. We then treated them with FGF4 and Wnt agonist to obtain posterior foregut spheroids. To shift into a three-dimensional culture, we embedded these spheroids in Matrigel, followed by pulse of retinoic acid (RA) during the early stage of organoid formation. The cells were further cultured in a hepatic differentiation medium for up to about one month, resulting in the generation of liver organoids (Figure 1A).

We next counted the number of organoids and measured the levels of albumin secretion with an ELISA of the collected medium samples. We integrated the undifferentiated iPS cell proliferation data that was obtained using the CM20 monitor and analyzed the correlation between the characteristics during the maintenance culture and the organoid differentiation efficiency of each iPS cell line (Figure 1B).

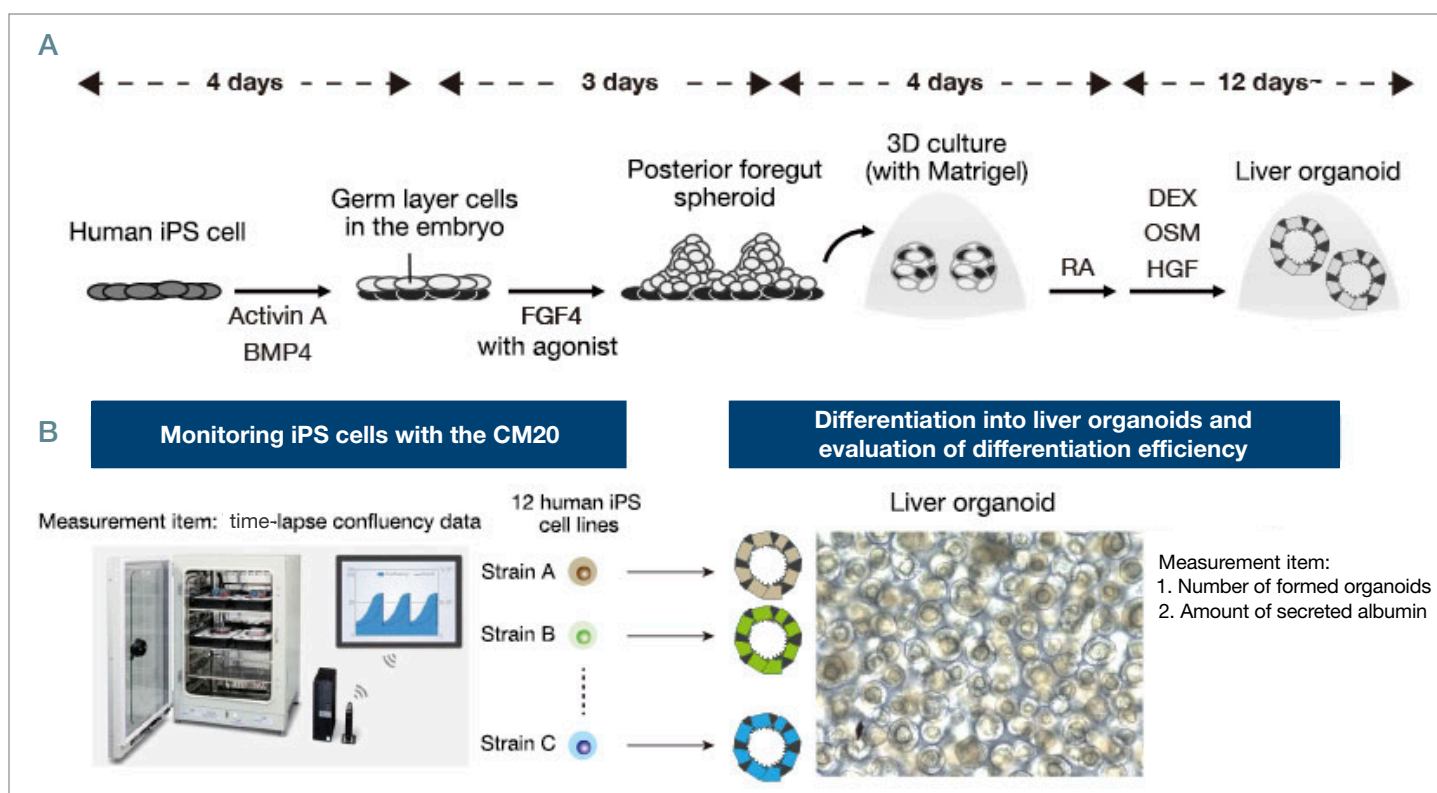


Figure 1. Monitoring human iPS cells during maintenance culture and evaluating liver organoid differentiation efficiency. (A) The culture protocol used to differentiate human iPS cells into liver organoids.

(B) Summary of comparative analysis of characteristics during iPS cell maintenance and liver organoid differentiation efficiency across 12 iPS cell lines derived from different donors.

Throughout multiple attempts to induce 12 human iPS cell lines to differentiate into liver organoids, we were able to obtain organoids from most of the cell lines. However, iPS cell lines I and J often failed to differentiate (Figure 2A). Although the albumin secretion (the amount of secretion per organoid) varied depending on the differential induction batch, the liver organoids derived from I and J iPS cell lines—which have extremely low organoid formation efficiency—also showed low levels of albumin secretion (Figure 2B). Among the cell lines with high organoid formation efficiency, we noticed some iPS cell lines, such as line C, showing relatively low albumin secretion. To further validate the differentiation, we confirmed that liver organoids derived from iPS cell lines other than I and J expressed hepatocyte-specific markers (data not shown). These data suggested that among the 12 cell lines tested, I and J iPS cell lines have restricted capacity to differentiate into the liver lineage.

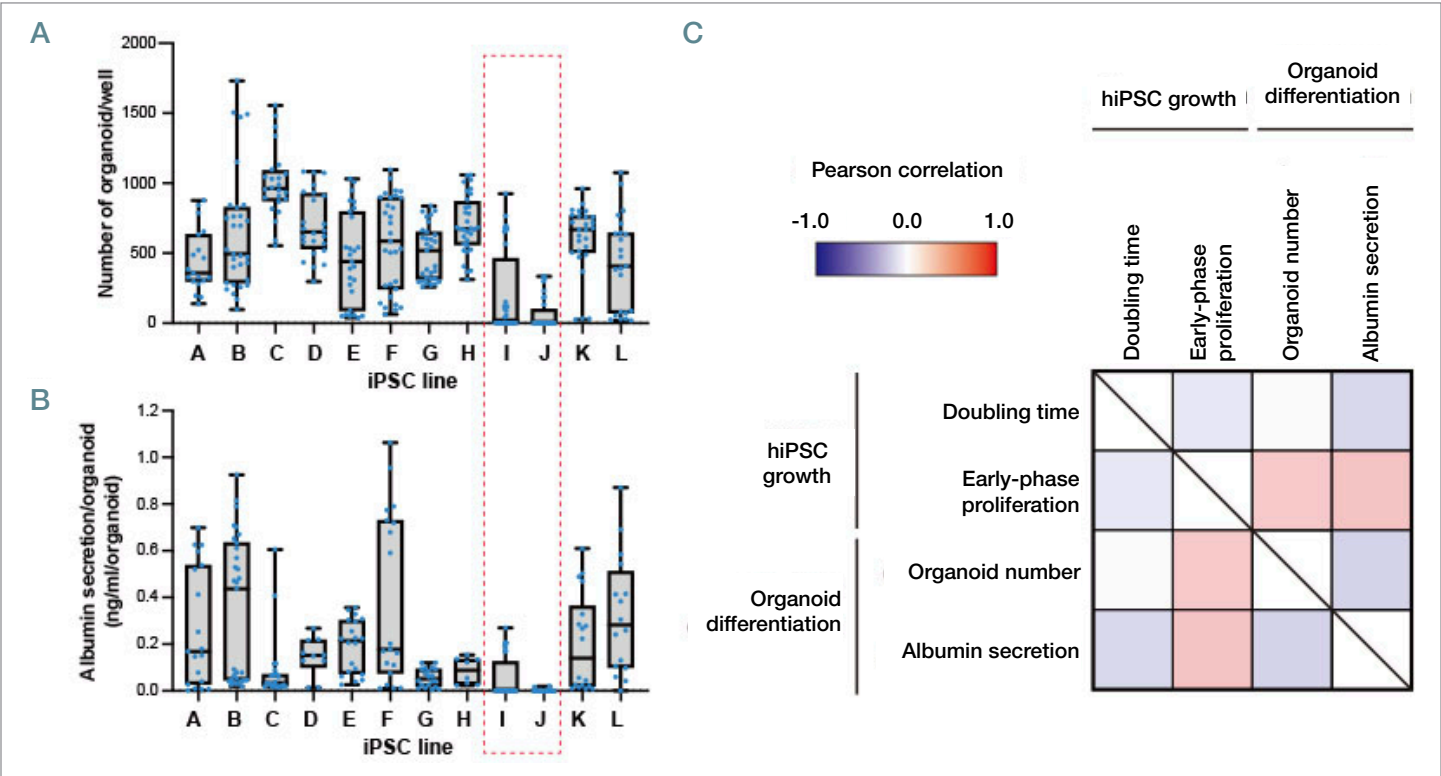


Figure 2. Correlation analysis of cell proliferation before differentiation induction and the efficiency of liver organoid differentiation across human iPS cell lines. (A, B) The number of liver organoids formed during the multiple differentiation induction experiments (A) and the level of albumin secretion (B) were plotted in a box plot for each iPS cell line. Blue dots correspond to the number of wells measured during multiple independent experiments. (C) The correlation map showing growth parameters of human iPS cells during maintenance (doubling time and early-phase proliferation) and liver organoid differentiation (organoid number and albumin secretion).

Next, to investigate whether the state of iPS cells before the differentiation induction step affects the liver organoid differentiation efficiency, we analyzed the correlation of the proliferation parameters acquired by the CM20 monitor, the number of formed organoids, and albumin secretion corresponding to each differentiation induction experiment. We calculated correlation coefficients between the iPS cell doubling time before differentiation induction (calculated using confluency data provided by the CM20 monitor), the growth efficiency at the initial stage of proliferation (calculated from a formula defined by Dr. Takebe), the number of generated liver organoids, and the levels of albumin secretion for each experiment. We accounted for batch-dependent variations by analyzing the dataset of each experiment (Figure 2C). While the number of generated liver organoids and the levels of albumin secretion showed almost no correlation with the iPS cell doubling time, they were positively correlated with the parameters of proliferation efficiency in the early stage of iPS cell proliferation. This indicates that although simple differences in doubling time between iPS cell lines cannot be used to determine whether the liver organoids generated are good or bad in their qualities, it is possible that some differences at the early stages of iPS cell proliferation observed between cell lines affect the efficiency of subsequent liver organoid differentiation.

Conclusion

The CM20 monitor's quantitative data enabled us to look at information from past cell cultures up to and even after differentiation into organoids. The images and data are easy to export, enabling a variety of analyses that can lead to new insights during the culture process.

In this study, we found that the variable efficiencies of liver organoid differentiation across iPS cell lines may be significantly affected by the growth efficiency of the iPS cells during their maintenance, particularly in the early stage of growth. This suggests that to generate more stable and higher quality liver organoids, it is important to monitor the state of iPS cells immediately after passage to know whether they are ready for differentiation induction. Based on this correlation, it is also possible to predict when a cell line will have good or poor differentiation efficiency by monitoring the proliferative state of iPS cell lines.

Olympus will continue research using the CM20 monitor to develop methods for efficient quality control and data management.

Comments from Dr. Takebe and Dr. Yoneyama

While handling multiple iPS cell lines derived from different donors and evaluating the differences between donors using iPS cell-derived organoids, we frequently encounter the problem that differentiation efficiency varies among iPS cell lines. The advantages of the CM20 monitor, including stable monitoring of proliferation states and the ability to export the data, were very helpful for us to perform the correlation analysis between the proliferation of iPS cell lines and differentiation efficiency of the generated organoids in 12 cell lines tested simultaneously.



Dr. Takanori Takebe (left)
Dr. Yosuke Yoneyama (right)
Tokyo Medical and Dental University
Institute of Research

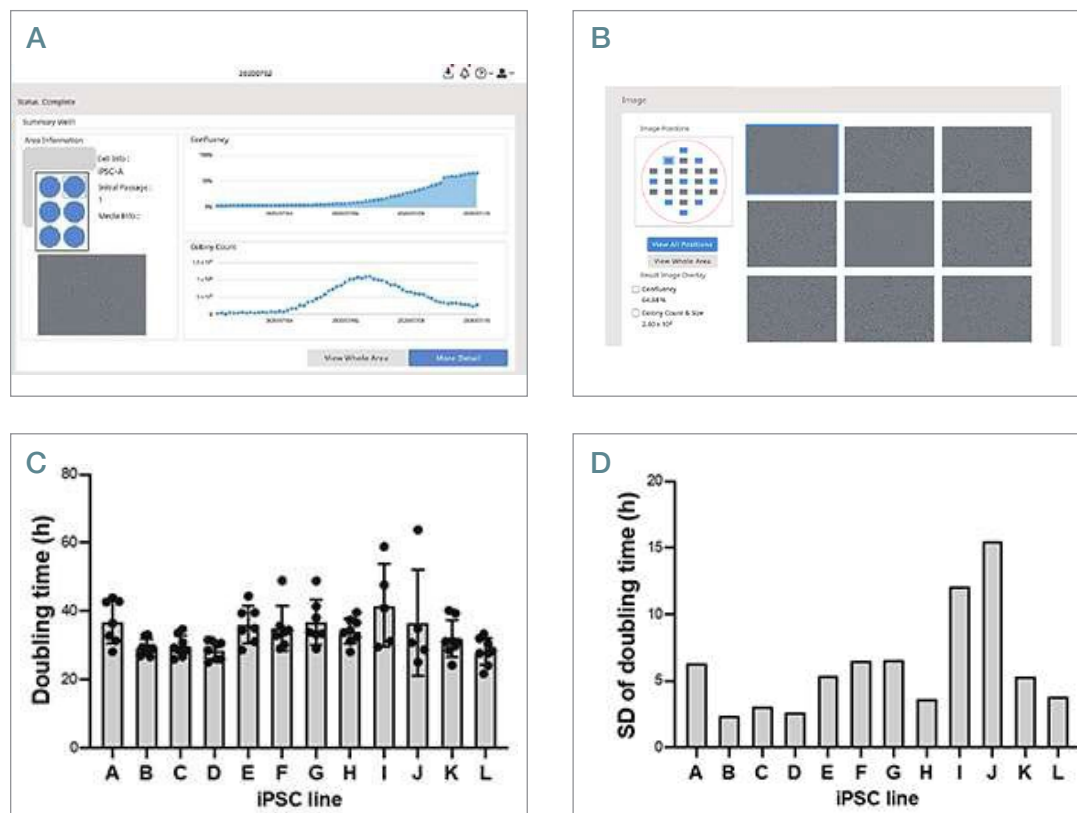
References

- *1) Takebe, T, Yoneyama, Y. Comparing Human iPS Cell Lines using the CM20 Incubation Monitoring System: Observing Differentiation into iPS Cell-Derived Liver Organoids. Olympus Life Science. <https://www.olympus-lifescience.com/en/applications/ips-comparative-analysis/>.
- *2) Ouchi R, Togo S, Kimura M, Shinozawa T, Koido M, Koike H, Thompson W, Karns RA, Mayhew CN, McGrath PS, McCauley HA, Zhang RR, Lewis K, Hakozaki S, Ferguson A, Saiki N, Yoneyama Y, Takeuchi I, Mabuchi Y, Akazawa C, Yoshikawa HY, Wells JM, Takebe T. Modeling Steatohepatitis in Humans with Pluripotent Stem Cell-Derived Organoids. *Cell Metabolism*, 30(2): 374–384 (2019)

Images of human iPS cells were acquired by the CM20 monitor on days 1, 4, and 7 after passage. The blue area was identified by the monitor's automatic colony recognition function.

For the 12 human iPS cell strains, the growth process during 5 to 8 passages was continuously monitored with the CM20 system (Fig. 2 A, B). These iPS cell lines underwent medium exchange and subculture at the same time. We found that each iPS cell proliferated in a doubling time of about 30 hours, and the proliferation speed was slightly different between iPS cell lines. We also found that among the human iPS cell lines, there are iPS cell lines (such as B strain and C strain) whose doubling time is almost constant between passages. This confirms that culture processes, such as medium replacement and subculture, were performed correctly (Fig. 2C).

On the other hand, some iPS cell lines, such as strain I and strain J, showed large variations in doubling time for each passage (Fig. 2D). These results demonstrate that the 12 iPS cell lines have different growth properties.



- A. CM20 monitor software interface.
- B. Single-well observation using the CM20 monitor. Images of 9 fields of view in the wells are acquired every 3 hours, and all well scans are automatically performed every day.
- C. The doubling time for each passage performed multiple times is plotted for each iPS cell line. The mean \pm standard deviation (SD) is shown in the bar graph.
- D. The variation in doubling time for each iPS cell line are shown in SD.

Quantitative analysis advantages

In the past, it was difficult to determine the causes of variation in the cell culture process when the quality varied. In particular, many studies using iPS cells require a lot of work to obtain the desired differentiated cells. It was difficult to measure how changes that can occur during iPS culture maintenance affect differentiated cells' evaluation results.

Because the CM20 monitor collects quantitative data on the cell growth process, data from different cell lines can be measured and compared using the same standards. The monitor makes it easy to collect data from multiple strains maintained by a single researcher and multiple researchers. By comparing the quantitative culture data, it is possible to determine whether there was a problem with the process or whether abnormal cells had been cultivated.

Olympus will continue research using the CM20 monitoring system to develop methods for efficient quality control and data management.

Comment from Dr. Takebe and Dr. Yoneyama

With the CM20 monitor, which can be permanently installed in the incubator, 6 to 12 iPS cell strains can be constantly monitored simply by placing the culture vessel or plate on the monitor. The growth data is captured and recorded without having to remove the cells from the incubator. It was useful for acquiring data on the differences between the cell lines. In addition, it takes a lot of effort to manually take photos of multiple stocks over time, but one of the advantages of the CM20 monitor is that it automatically stores and organizes the photos.



Dr. Takanori Takebe (left)
Dr. Yosuke Yoneyama (right)
Tokyo Medical and Dental University
Institute of Research

Breakthrough in Live Cell Microscopy of 3D Cellular Models

A new method enables high-resolution 3D live cell microscopy for medium throughput compound screening

Introduction

In many applications of drug discovery and basic research, classical 2D cell cultures (monolayer of cells on coated coverslips or in multiwell plates) are currently replaced by more complex 3D cellular models. These models comprise, for example, spheroids grown from tumors, intestinal or brain cells, organ explants, or complex cellular co-cultures.

Because of their size in both the lateral and axial directions, live cell microscopy at cellular or even subcellular resolution is challenging using conventional techniques such as widefield fluorescence microscopy and laser-scanning confocal or spinning-disk microscopy. Even lightsheet microscopy, which has been successfully applied to imaging of zebrafish larvae, cannot be used as a universal tool for imaging of 3D cellular models. Depending on the microscope type that is used for imaging, challenges include phototoxicity⁽¹⁾, insufficient axial resolution, or the need for special equipment for sample-mounting^(2,3). In a collaboration of Novartis and Olympus, a modified version of an inverted multiphoton microscope was developed to address the needs of high-resolution longterm 3D time-lapse imaging of 3D cellular models. Several key challenges had to be addressed in this project: a dual-line 2P laser is needed to enable simultaneous excitation of at least two fluorochromes. Secondly, a long working distance (4 mm) water immersion lens with high numerical aperture (NA) of at least 1.0 needs to be used for creating image stacks with sufficient axial resolution. Administration of substances by microfluidic perfusion also needs to be included for efficient compound administration and buffer-exchange. The FLUOVIEW™ FVMPE-RS system discussed here allows efficient 3D imaging of cell cultures grown in standard 24- to 96- well plates over several days and bridges the gap between research microscopes and high-content imaging systems. At Novartis the system is routinely used for medium-throughput compound profiling assays, including studies on tumour and liver spheroids, muscle, skin, and intestinal tissue explants as well as various co-cultures.



FLUOVIEW FVMPE-RS System Benefits

The FVMPE-RS advanced, turnkey multiphoton microscope enables deep imaging in biological tissues.

- 1 Capture fast dynamics in live tissue
- 2 Obtain bright images from deep within highly scattering specimens
- 3 Image up to 8 mm into cleared tissues

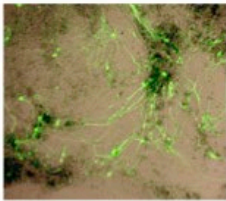
Muscle/nerve	Muscle	Skin	Tumor	Brain
iPS derived models	Printed muscle fibers	Reconstituted skin	Breast cancer spheroids	Organoids / mini-brains
				
Formation of NMJ's	Calcium signaling and force generation	Wound healing	Treatment studies	Formation of neuronal networks

Figure 1. Examples for 3D complex cellular models for studying basic biology questions and compound effects.

Classical assay formats based on 2D cell cultures

For many decades, cells have been plated in Petri dishes or placed in multiwell plates for basic biological studies or to test the effect of compounds on cell function or phenotype. It is often very apparent that plating cells on plastic or glass usually yields phenotypically different cells than under *in vivo* conditions, even when the plates are coated with a mixture of proteins such as laminin, Matrigel, or collagen. In many cases, cells tend to spread out and form extensions that form strong bonds with the coating. Moreover, studies on mechanotransduction in cells found clear evidence that cells perceive the stiffness of their environment and as a result adapt their molecular pathways, function, and phenotype^(4, 5). Therefore, the use of 2D cultures has limited translational value, and often results obtained in the *in vitro* cellular model do not fully correlate with findings in animal models or human subjects.

3D cellular models for creating enhanced translational value

As an alternative to 2D cell cultures, great efforts have been undertaken in recent years to develop 3D cellular models. The biology of these models seem to match better to the *in vivo* situation in terms of gene expression, pathway regulation, and phenotype^(6–8). These 3D models consist of cell clusters (organoids, spheroids) ranging in size from about 150 to 300 μm . They may contain one or more cell types and can be embedded in different extracellular matrices. These cell models are grown in microwell plates with 24 to 96 wells or in special microfluidic chips (Figure 1).

The limitations of fluorescence microscopy in 3D imaging

A wide range of microscopic techniques are available for studying 3D cellular models in the lab dish. Although not suited for true 3D imaging, widefield fluorescent microscopy can serve as an entry point to quantitative analysis. In applications where only the size of the spheroid or the global level of fluorescence is of relevance for the project, widefield imaging can even offer particular advantages over more sophisticated technologies because of its very fast image acquisition and minimal phototoxicity.

A variety of different laser-based methodologies allow “real” 3D imaging

- In confocal laser scanning microscopy, a laser beam focused by the objective scans the specimen point by point. The emission is filtered by a pinhole and analyzed by using a photo-multiplier tube (PMT).
- In spinning disk confocal microscopy, multiple image points are simultaneously excited, and the data is acquired using a camera with high sensitivity. This makes spinning disk microscopy suitable for studying dynamic cellular processes in living cells at high speed. The effective exposure of the living cells to the laser light is slightly lower than in confocal laser scanning microscopy because of higher photon efficiency of the detector.
- Single plane illuminated microscopy (SPIM, also referred to as lightsheet microscopy) is based on selective illumination of a thin plane. A camera captures images of the plane at high speed. Phototoxicity and bleaching effects are also extremely low. In the past, the method became very popular for studying the development of zebrafish embryos^(3, 9).

The next level: multiphoton microscopy

Visible light as used by the above-mentioned techniques for single-photon-fluorescence excitation undergoes absorption and scattering in living tissue. In the majority of applications, cellular resolution can only be achieved in areas not more than 50–100 μm away from the surface. In 2-photon microscopy, excitation of the dye occurs by simultaneous absorption of two photons of longer wavelength⁽¹⁰⁾. To give an example, for excitation of the green-fluorescent-protein, a 480nm continuous-wave laser is used for single photon (confocal or spinning disk) laser scanning microscopy, and 900nm light emitted by a pulsed laser is used for 2-photon excitation. Another important advantage of 2-photon over single-photon excitation is the smaller volume of excitation. The 2-photon effect can just occur in the focal spot of the objective, where the photon flux is very high. In single photon microscopy, however, excitation occurs also above and below the focal plane leading to much higher phototoxicity. Advantages of 2-photon over single-photon excitation can also be seen on the detector side: a pinhole is used in single-photon excitation to filter out all photons that have been generated outside of the focal plane. Because photon emission occurs in all directions, many photons will not be detected as they do not pass through the pinhole. Moreover, photons that were emitted in the direction of the detector, but which have undergone scattering, might not be detected. These technical and physical constraints lead to a rather low photon-detection efficiency. Finally, photon scattering can also lead to “out-of-focus” light. Here, photons that have been generated outside of the focal plane were scattered within the tissue to pass through the pinhole. This effect will cause blurring within the image and becomes particularly prominent at high signal intensity.

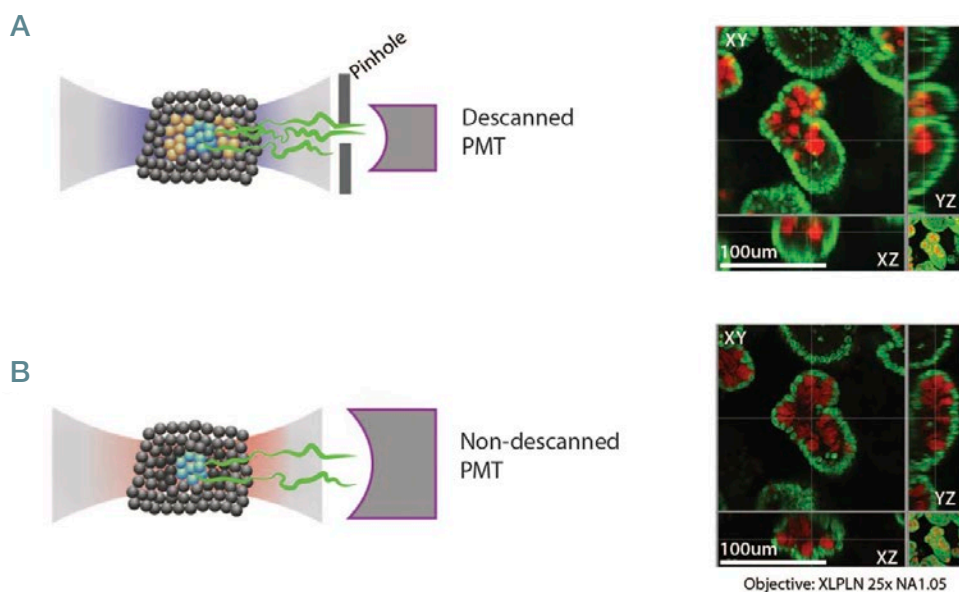


Figure 2. Difference in image quality comparing one- and two-photon-excitation for intestinal crypts. Nuclei were stained with DAPI (green) and stained lysozyme is shown in red. A) One-photon-excitation with confocal detection. Excitation is not confined to the focal area of the objective (blue) but dye molecules are also excited in adjacent areas (out-of-focus-light, yellow) along the laser beam. Scattering of photons on both the excitation and emission level lead to reduced sharpness and loss of signal intensity. B) Two-photon-excitation (2PE). Two-photon-excitation can only occur if the light intensity of the laser exceeds a certain threshold. Therefore, 2PE does not lead to any out-of-focus light. In addition, the non-descanned detector has a larger surface area and is located closer to the back focal plane of the objective. Hence, it will capture photons from a wider range of angles. Images acquired with two-photon excitation appear less blurred and show more detail. 3D image stacks were acquired using a 25x, NA1.05 objective.

In 2-photon microscopy, a pinhole is not needed because photons can just be generated within the focal plane. This allows placing the detector much closer to the objective. Usually, the diameter of the photo-multiplier is also larger allowing detection of photons from a large area at the back focal plane of the objective.

Generation of reactive oxygen species (ROS) and photodamage of cells is also of less concern in 2-photon-microscopy. Although laser power is larger compared to single-photon-microscopy, cells seem to be able to eliminate ROS more efficiently because generation of long-lived triplet excited oxygen occurs in a much smaller excitation volume^(11–13).

The numerical aperture (NA) of an objective determines its lateral and axial point-spread-function (PSF) and its resolution within the image plane and across a 3D image stack. In 2D imaging the lateral resolution is the most relevant, and high-quality images with subcellular resolution can already be obtained with a low NA. However, in 3D imaging the axial PSF is of critical importance. While in an ideal system the axial PSF is only about two times larger compared to the lateral PSF, spherical aberrations caused by refractive index mismatch in deep tissue imaging lead to additional distortions and widening of the axial PSF. Therefore, experiments need to be carried out using objectives with $NA > 1$ to obtain high-quality 3D image stacks.

The images shown in Figure 4 were either obtained with a conventional dry objective with low NA or the Olympus XLPLN 25x, NA 1.05 (2.0 mm working distance) dedicated water immersed 2-photon objective. While the lateral resolution appears to be sufficient in both examples, the axial resolution is only large enough to identify cells in the x-z- or y-z-plane when the high NA objective was used. At low NA, cells appear as sticks and not as roundish objects.

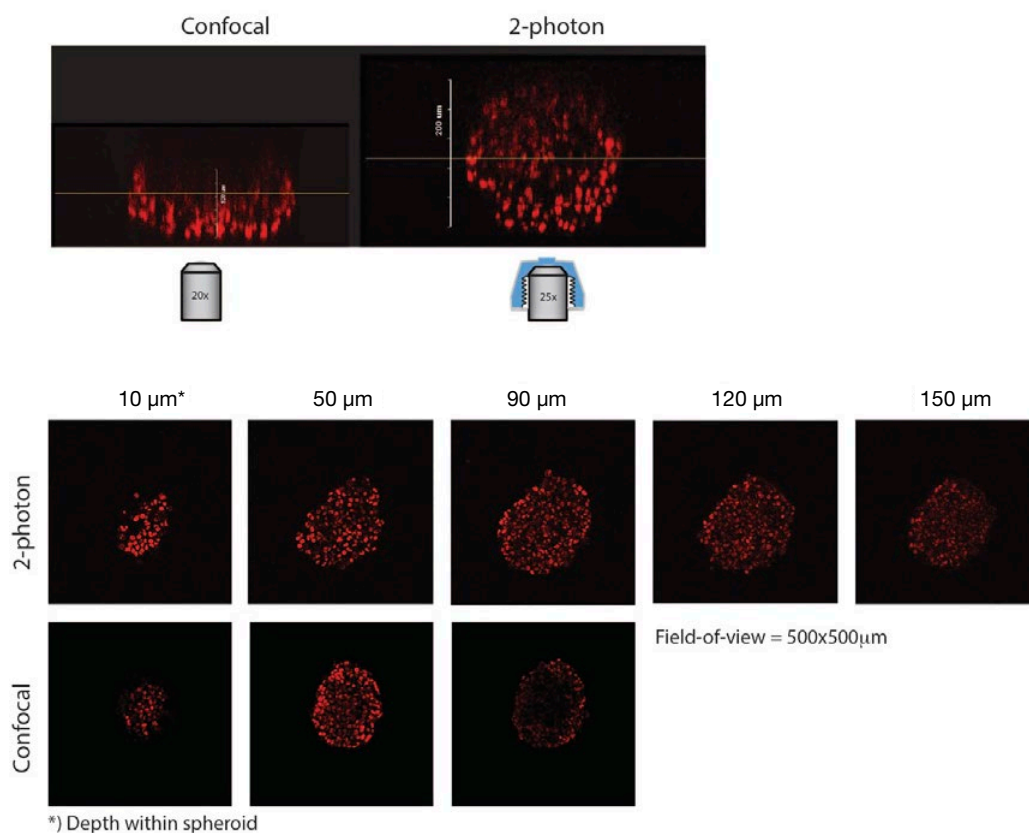


Figure 3. Comparison of confocal with 2-photon-microscopy. This comparison illustrates the difference in penetration depth of visible light (570 nm, confocal microscopy) with infrared light (1024 nm, 2P-excitation, XLPLN25XSVM2 objective lens with WD 4 mm and NA 1.0). While images with sufficient signal intensity can only be obtained from the outer 50 μm in confocal images, penetration depth exceeds 150 μm for 2P-excitation at a wavelength of 1024 nm. The panel on the top shows an x-z-projection of the 3D dataset for both techniques. The lower panel shows individual images at different levels within the spheroid.

Implementation of multiphoton microscopy on an inverted stage

Historically, multiphoton microscopy was implemented on an upright stage tuned for intravital microscopy in living animals to study brains, spinal cords, tumors, or lymph nodes. This setup is not very well suited for imaging cell culture plates because the stage cannot easily move from well to well if the lens approaches the sample from the top. However, technically it is feasible to mount a tuneable 2-photon laser onto an inverted microscopy stage. In most applications, cells are stained with at least two different dyes (e.g., one to identify the outline of a cell and another one used as a functional biosensor). It is important that at least two dyes or fluorescent proteins can be excited at the same time. Lasers such as the Spectra-Physics InSight DeepSee offer one laser line that can be tuned between 690 and 1300 nm and a second line at a fixed wavelength of 1040 nm. With this combination it is possible to excite two dyes, such as GFP (900 nm) and RFP (1024 nm), simultaneously, which allows scientists to design smarter experiments.

Another challenge for using multiphoton microscopy on an inverted microscope is the application of an immersion fluid to fill the gap between the bottom of the wellplate and the front lens of the objective. While closing this gap using a funnel-like adaptor is possible for short working distance lenses, it becomes a real challenge if the working distance exceeds 1–2 mm. The water film that is only kept between the two ends by surface tension needs to be resistant to moving the plate over the objective and axial movements over millimeters. To address this challenge the microscope stage had to be equipped with a specially developed immersion bridge that enables the use of 8 mm working distance lenses (Figure 5).

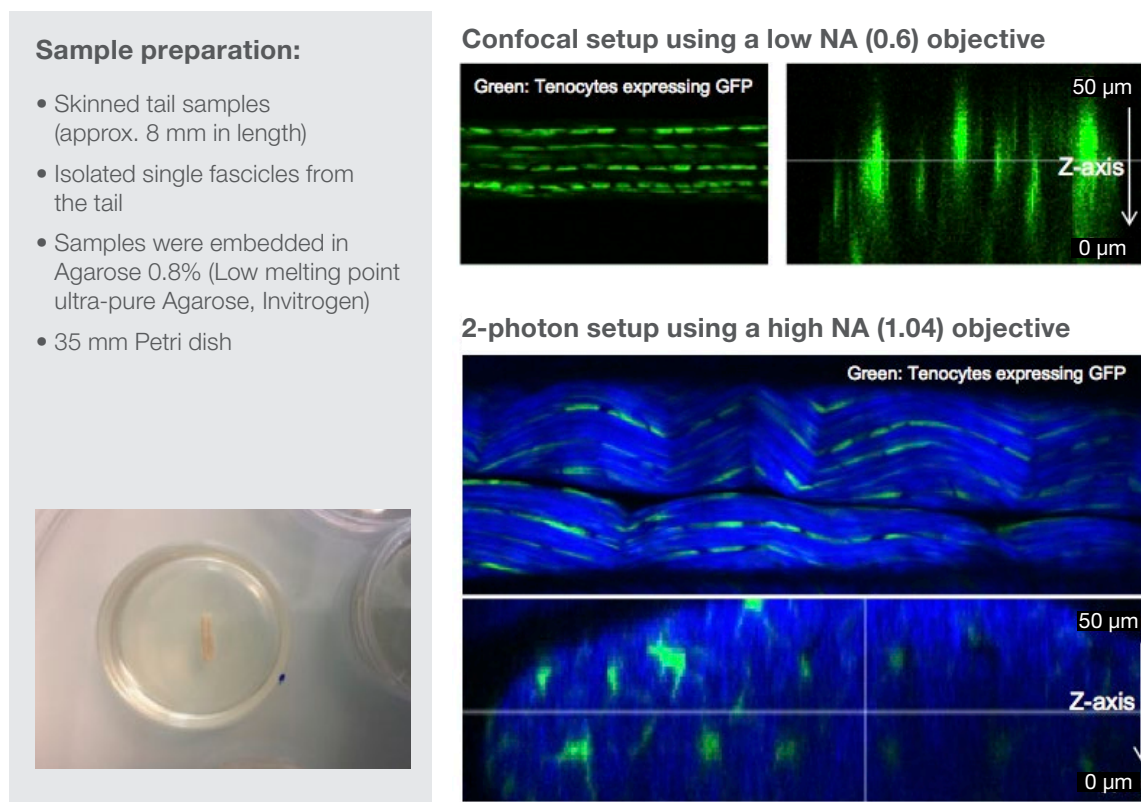
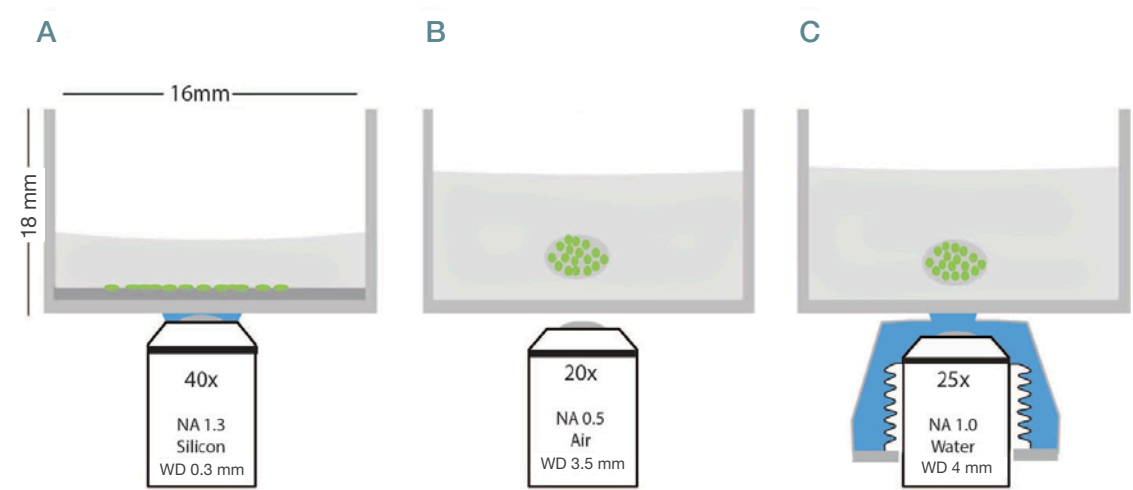


Figure 4. Imaging of tendon samples using either a low or high NA objective in combination with 2P excitation. The cells were expressing GFP. The images obtained with the high NA objective also show the second-harmonic-signal generated by the collagen. The samples were embedded in 0.8% agarose in a 35 mm Petri dish.

Compound administration

The way compounds are administered to cell cultures is fundamentally different in basic research projects and compound screening. If the number of wells is small—for example, if cells are studied in a single Petri dish or 24-well plate—compounds can be added by using a manual pipette. This can be done shortly before imaging starts or by pausing data acquisition after baseline images have been recorded. One caveat of this procedure is that cells can be displaced by touching the well with the tip of the pipette or by adding the fluid too quickly. Because of the large number of samples in high-content imaging, compounds need to be applied using dedicated fully multiplexed dispensers (14). This usually occurs before the start of the experiment and outside of the microscope. Thousands of compounds can be studied in batch mode, but analysis of the kinetics of the pharmacodynamic (PD) effect is almost impossible. Imaging of the PD effect is linked to an endpoint measurement, such as cell death.

By using microfluidic compound administration techniques, we have started to develop a system where compounds can be administered to the samples in a tightly controlled and dynamic fashion. In our setup, we are using microfluidic pressure-driven pumps that allow administration of compounds at a given concentration into up to 24 wells at flow rates ranging practically from 5–20 $\mu\text{l/min}$. Using microfluidic chip technology, it is even possible to serialize compound administration to several replicates and create data sets with higher statistical power (15).



Vendor-specific examples of objectives used in life science applications

UPLSAPO 40XS		UPLSAPO 20x		XLPLN25XSVM2	
Magnification	40	Magnification	20	Magnification	25
Numerical aperture (NA)	1.25	Numerical aperture (NA)	0.75	Numerical aperture (NA)	1
Working distance [mm]	0.3	Working distance (WD) [mm]	0.6	Working distance (WD) [mm]	4

Figure 4. Conceptual differences for imaging 2D and 3D cellular models. Very often 24-well plates are used, for which spatial dimensions are indicated in A. (A) Objectives with short working distances are used in combination with water or silicone oil to achieve high numerical aperture (NA) and good refractive index matching. (B) The distance between the objective and the object can be in the range of several mm in many 3D cellular models. In a conventional microscopy setup, only dry lenses can be used, as the immersion fluid cannot be kept between front lens and the plate. As a consequence, NA will be significantly lower, leading in particular to dramatically reduced axial resolution. (C) In specialized setups, the immersion fluid can constantly be applied even if long working distance lenses are used. High NA can be achieved by using dedicated objectives developed for MPM applications.

Conclusions

In the past, analysis of 3D cellular models at good resolution was challenging, particularly during time-lapse imaging in multiwell plates. Using a modified inverted microscope, it is possible to efficiently address basic biology questions as well as compound effects in 3D cellular models. The multiphoton microscope presented here bridges the gap between high-content imaging and a classical research microscope. While the optical quality of the image data is certainly outstanding, the throughput is limited, allowing scientists to study approximately 20–40 spheroids in one hour at isotropic micro-meter resolution. This trade-off will be acceptable in many projects where only a few compounds should undergo in-depth profiling. For larger screening studies, dedicated high-content-imaging systems will still be the technology of choice. However, future improvements in hardware design as well as smarter microscopy-control-software will certainly enhance the output of high-end-microscopes and open up new opportunities for their use in drug discovery.

Authors

Bülent Peker, PhD
Senior Product Manager
Laser Scanning Microscopes
Scientific Solutions Division
Olympus Europa SE & Co. KG Hamburg,
GERMANY

Martin Rausch, PhD
Director Microscopy and BioPhotonics Group
Analytical Sciences and Imaging
Novartis Institutes for Biomedical Research
Basel, SWITZERLAND

References

1. Dailey, M.E., E. Manders, D.R. Soll, and M. Terasaki. 2006. Confocal microscopy of living cells. *Handb. Biol. Confocal Microsc.* Third Ed.: 381–403.
2. Pampaloni, F., U. Berge, A. Marmaras, P. Horvath, R. Kroschewski, and E.H.K. Stelzer. 2014. Tissue-culture light sheet fluorescence microscopy (TC-LSFM) allows long-term imaging of three-dimensional cell cultures under controlled conditions. *Integr. Biol. (Camb)*. 6: 988–98.
3. Keller, P.J., A.D. Schmidt, J. Wittbrodt, and E.H.K. Stelzer. 2008. Reconstruction of zebrafish early embryonic development by scanned light sheet microscopy. *Science* (80-). 322: 1065–1069.
4. Wells, R.G. 2008. The role of matrix stiffness in regulating cell behavior. *Hepatology*. 47: 1394–1400.
5. Levental, I., P.C. Georges, and P.A. Janmey. 2007. Soft biological materials and their impact on cell function. *Soft Matter*. 3: 299–306.
6. Riedl, A., M. Schleiderer, K. Pudelko, M. Stadler, S. Walter, D. Unterleuthner, C. Unger, N. Kramer, M. Hengst-schläger, L. Kenner, D. Pfeiffer, G. Krupitza, and H. Dolznig. 2017. Comparison of cancer cells in 2D vs 3D culture reveals differences in AKT–mTOR–S6K signaling and drug responses. *J. Cell Sci.* 130: 203–218.
7. Howes, A.L., R.D. Richardson, D. Finlay, and K. Vuori. 2014. 3-Dimensional culture systems for anti-cancer compound profiling and high-Throughput screening reveal increases in EGFR inhibitor-mediated Cytotoxicity compared to monolayer culture systems. *PLoS One*. 9.
8. Duval, K., H. Grover, L.-H. Han, Y. Mou, A.F. Pegoraro, J. Fredberg, and Z. Chen. 2017. Modeling Physiological Events in 2D vs. 3D Cell Culture. *Physiology*. 32:266–277.
9. Pantazis, P., and W. Supatto. 2014. Advances in whole-embryo imaging: a quantitative transition is underway. *Nat. Rev. Mol. Cell Biol.* 15: 327–39.
10. Denk, W., J.H. Strickler, and W.W. Webb. 1990. Two-photon laser scanning fluorescence microscopy. *Science*. 248: 73–6.
11. Squirrell, J.M., D.L. Wokosin, J.G. White, and B.D. Bavister. 1999. Long-term two-photon fluorescence imaging of mammalian embryos without compromising viability. *Nat. Biotechnol.* 17: 763–7.
12. Patterson, G.H., and D.W. Piston. 2000. Photobleaching in two-photon excitation microscopy. *Biophys. J.* 78:2159–62.
13. Diaspro, A., G. Chirico, C. Usai, P. Ramoino, and J. Dobrucki. 2006. Photobleaching. *Handb. Biol. Confocal Microsc.* : 690–702.
14. Sackmann, E.K., L. Majlof, A. Hahn-Windgassen, B. Eaton, T. Bandzava, J. Daulton, A. Vandenbroucke, M. Mock, R.G. Stearns, S. Hinkson, and S. S. Datwani. 2016. Technologies That Enable Accurate and Precise Nano- to Milliliter-Scale d Dispensing of Aqueous Reagents Using Acoustic Droplet Ejection. *J. Lab. Au-tom.* 21: 166–177.
15. Lohasz, C., N. Rousset, K. Renggli, A. Hierlemann, and O. Frey. 2018. Scalable Microfluidic Platform for Flexible Configuration of and Experiments with Microtissue Multiorgan Models. *SLAS Technol. Transl. Life Sci. Innov.* : 247263031880258.

An In Vitro System for Evaluating Molecular Targeted Drugs Using Lung Patient-Derived Tumor Organoids

Abstract

Patient-derived tumor organoids (PDOs) represent a promising preclinical cancer model that better replicates disease, compared with traditional cell culture models. We have established PDOs from various human tumors to accurately and efficiently recapitulate the tissue architecture and function. Molecular targeted therapies with remarkable efficacy are currently in use against various tumors. Thus, there is a need for in vitro functional-potency assays that can be used to test the efficacy of molecular targeted drugs and model complex interactions between immune cells and tumor cells to evaluate the potential for cancer immunotherapy. This study represents an in vitro evaluation of different classes of molecular targeted drugs, including small-molecule inhibitors, monoclonal antibodies, and an antibody-drug conjugate, using lung PDOs. We evaluated epidermal growth factor receptor and human epidermal growth factor receptor 2 (HER2) inhibitors using a suitable high-throughput assay system. Next, the antibody-dependent cellular cytotoxicity (ADCC) activity of an anti-HER2 monoclonal antibody was evaluated to visualize the interactions of immune cells with PDOs during ADCC responses. Moreover, an evaluation system was developed for the immune checkpoint inhibitors nivolumab and pembrolizumab using PDOs. Our results demonstrate that the in vitro assay systems using PDOs were suitable for evaluating molecular targeted drugs under conditions that better reflect pathological conditions.

Keywords

Molecular targeted therapy; cancer immunotherapy; cancer immunity; molecular targeted drugs; antibody drug; antibody-drug conjugate; immune checkpoint inhibitor; patient-derived tumor organoid; antibody-dependent cellular cytotoxicity; 3D cell-analysis system

Introduction

Molecular targeted therapy is one of the most important paradigm shifts in the history of cancer therapy. Traditional anticancer chemotherapeutic agents block cell division and DNA replication, and reduce the size of tumors. Although chemotherapeutic agents lead to an extension of patients' overall survival, they are not effective for all types of cancer and induce side effects. Recently, molecular targeted drugs have been developed that interfere with specific molecules to block cancer growth, progression, and metastasis (1–3). Many molecular targeted drugs have demonstrated remarkable clinical success in treating myriad types of cancer, including breast, leukemia, colorectal, lung, and ovarian cancer. In addition, targeting the immune system, which accelerates anti-tumor activity through immune checkpoint inhibition, is proving to be an increasingly effective method for treating various cancers, prolonging life, and increasing progression-free survival (1–3). However, molecular targeted approaches continue to be limited by wide variations in the degree and durability of patient responses and side effects, and numerous cancers remain completely refractory to such therapy. Thus, molecular targeted therapy needs further improvement for greater clinical efficacy.

Historically, human cancer cell lines have been widely used for studies as preclinical models to evaluate anticancer agents. However, these models may not reflect the characteristics of the source tumor tissues *in vivo* as they are frequently passaged for long periods of time, which may lead to alterations in their genome sequences, gene-expression profiles, and morphologies. In addition, almost all cell lines are cultured under monolayer conditions or used as xenografts in mice, which is not physically representative of tumor tissues (4,5). Therefore, the results of evaluations performed with cancer cell lines do not accurately predict the clinical effects of anticancer drugs. Indeed, ~85% of preclinical agents entering oncology clinical trials fail to demonstrate sufficient safety or efficacy required to gain regulatory approval (6–8). *In vitro* systems, including patient-derived tumor cell, organoid, or spheroid models that accurately recapitulate tissue architecture and function, have been developed for various types of tumor tissues (e.g., colon, lung, pancreatic, prostate, endometrial, liver, bladder, breast, brain, kidney, endometrium, and stomach), as have high-throughput assay systems for using these systems (9–20). These models are promising in terms of facilitating a better understanding of cancer biology and for evaluating drug efficacy *in vitro*.

Previously, we established a novel series of patient-derived tumor organoids (PDOs) from various types of tumor tissues from the Fukushima Translational Research Project, which are designated as Fukushima (F)-PDOs. F-PDOs could be cultured for >6 months and formed cell clusters with similar morphologies to their source tumors (21). Comparative histological and comprehensive gene-expression analyses also demonstrated that the characteristics of PDOs were similar to those of their source tumors, even following long-term expansion in culture. In addition, suitable high-throughput assay systems were constructed for each F-PDO in 96- and 384-well plate formats. We suggest that assay systems based on F-PDOs may be utilized to evaluate anticancer agents under conditions that better reflect clinical conditions (compared with conventional methods using cancer cell lines) and to discover markers of the pharmacological effects of anticancer agents.

Although several cell-based assay systems using cancer cells have been developed for evaluating molecular targeted drugs, more efficient and simple cell-based assay systems for identifying clinically efficacious therapy potency are desired. To address this issue, we have attempted to construct efficient cell-based assays for evaluating molecular targeted drugs, including small molecules, monoclonal antibodies, and immune-checkpoint inhibitors using F-PDOs, which maintain the characteristics of their source tumors. In this study, epidermal growth factor receptor (EGFR) and human epidermal growth factor receptor 2 (HER2) inhibitors, including small molecules, monoclonal antibodies, and antibody-drug conjugates (ADCs) in clinical use, were evaluated using lung F-PDOs. EGFR is a tyrosine kinase receptor, and its activation triggers the activation several downstream pathways, including the RAS/mitogen-activated protein kinase (MAPK), phosphoinositide 3-kinase (PI3K)/Akt, and Janus kinase (JAK)/signal transducer and activation of transcription protein (STAT) pathways that regulate cell proliferation, survival, adhesion, migration, and differentiation (22–25). EGFR overexpression and EGFR-mediated signaling-pathway dysregulation have been observed in tumors from patients with several cancers, especially non-small cell lung cancer. Thus, several anti-EGFR drugs have been developed for clinical use in cancer therapy, including the small-molecule tyrosine kinase inhibitors (TKIs) gefitinib, erlotinib, afatinib, neratinib, dacomitinib, and osimertinib, as well as the monoclonal antibodies cetuximab and necitumumab [22–25]. In addition, HER2 can activate the same key signaling pathways as EGFR. Thus, HER2 is an ideal target for anticancer agents, and several HER2 inhibitors, including trastuzumab and pertuzumab (monoclonal antibodies); afatinib, lapatinib, and neratinib (TKIs); and trastuzumab emtansine (an ADC) have been developed and approved for clinical use (24,26). Therefore, we first evaluated the functional potency of several EGFR and HER2 inhibitors by high-throughput screening (HTS) using three lung F-PDOs (RLUN5, RLUN16, and RLUN21). Moreover, the antibody-dependent cellular cytotoxicity (ADCC) activity of trastuzumab was evaluated using three lung F-PDOs, and the complex interactions of immune cells with F-PDOs during ADCC responses to trastuzumab were visualized.

In addition, a system for evaluating immune-checkpoint inhibitors using lung F-PDOs was developed based on non-invasive, label-free, and real-time cellular impedance monitoring technology (xCELLigence) (27) to measure the potencies of biologics. Recently, Cerignoli et al. developed a real-time, impedance-monitoring system to assess immune-checkpoint inhibitors using prostate cancer PC3 cells, in combination with an anti-programmed cell death-1 (PD-1) antibody and peripheral blood mononuclear cells (PBMCs) (27). Therefore, we utilized the xCELLigence platform to investigate whether F-PDOs are also suitable for assessing the effects of checkpoint inhibitors on the immune system. Interactions between PD-1 expressed on the surface of activated T cells and its ligand PD-L1 on cancer cells inhibit the ability of T cells to attack the target cells. Immune-checkpoint inhibitors remove inhibitory signals of T-cell activation, which enables tumor-reactive T cells to overcome regulatory mechanisms and mount an effective antitumor response; thus, they are now used clinically for treating a broad range of tumor types (28,29). We selected the anti-PD-1 monoclonal antibodies nivolumab and pembrolizumab as representative immune-checkpoint inhibitors in this study.

2. Materials and Methods

2.1. Antibodies, Compounds, and Reagents

Trastuzumab, pertuzumab, and trastuzumab emtansine were purchased from Roche (Basel, Switzerland). Cetuximab and nivolumab were obtained from Bristol-Myers Squibb (New York, NY, USA). Pembrolizumab was provided by Merck & Co. (Kenilworth, NJ, USA). An anti-Ki-67 antibody (ab16667) was purchased from Abcam (Cambridge, UK).

Seventy-eight anticancer agents were tested in this study (Table S1). All compounds were dissolved in dimethyl sulfoxide at a concentration of 20 mM and stored at -80 °C (-112 °F) until use. The purity and integrity of the compounds were measured via ultra-performance liquid chromatography-mass spectrometry (Waters Corporation, Milford, MA, USA), using a 1-μL injection volume, as follows. A Waters CORTECS C₁₈ column (particle size: 1.6 μm; column size: 2.1 × 50 mm; Waters Corporation) was developed with a linear aqueous acetonitrile (MeCN) gradient containing a 0.1% formic acid (5–90% MeCN, 1.6 min; flow rate, 1 mL/min). Separation was performed at 40 °C (104 °F), and the components of the major ultraviolet (UV) adsorption peaks were verified by mass spectrometry (Table S1). Epidermal growth factor (EGF) and interferon- (IFN-) were obtained from Fujifilm Wako Pure Chemical, Ltd. (Osaka, Japan). Staphylococcal enterotoxin B (SEB) was obtained from Sigma-Aldrich (St. Louis, MO, USA).

2.2. Cells

All experiments with human material were performed in accordance with the guidelines of the Declaration of Helsinki and were approved in advance by the ethics committee of the Fukushima Medical University (approval number: 1953; approval date: 21 October 2018). Clinical specimens used for the PDOs were acquired from cancer patients at Fukushima Medical University Hospital after providing informed consent. Previously, we reported the establishment of 53 F-PDOs from human tumor tissues (21). Out of those PDOs, three lung F-PDOs (RLUN5, RLUN16, and RLUN21) were selected for use in this study. Briefly, RLUN5, RLUN16, and RLUN21 were each established from lung cancer tissues removed from the lung by surgery. As described previously (21), the cancer tissues were washed with Hank's balanced salt solution (Fujifilm Wako Pure Chemical, Ltd.) supplemented with penicillin-streptomycin solution (Fujifilm Wako Pure Chemical, Ltd.), cut with a scalpel into small pieces (approximately 1 mm³), and cultured in suspension for 3–6 months to establish the F-PDOs.

THP-1 cells were obtained from Japanese Collection of Research Bioresources Cell Bank (Osaka, Japan). PBMCs were provided by Precision Bioservices (Frederick, MD, USA).

2.3. Cell Culture

F-PDOs were cultured at 37 °C (98.6 °F) in 15 mL FBIM001 (21) using ultra-low attachment 75 cm² flasks (Corning, Inc., NY, USA) in a humidified incubator with 5% CO₂. Because accurate cell numbers of F-PDOs could not be determined using a cell counter, the volumes of cell pellets after centrifuging cell suspensions in 15 ml tubes were visually estimated by comparison with tubes marked at volumes of 75, 100, and 150 µL. The 80% medium was changed twice weekly. When F-PDOs reached their maximum saturation density, the cells were passaged at a 1:2 ratio. The procedure for handling F-PDOs was described in detail elsewhere (21). F-PDOs were cultured in flasks until sufficient cell-pellet volumes were obtained for the assay. For all experiments, the F-PDO culture media were replaced at 1 day prior to seeding, as previously described (21).

THP-1 cells were cultured in vendor-recommended growth media supplemented with fetal bovine serum (FSA; Sigma-Aldrich, St. Louis, MO, USA) and penicillin-streptomycin solution (Fujifilm Wako Pure Chemical, Ltd.) at final concentrations of 10% and 1%, respectively, at 37 °C (98.6 °F) in a humidified incubator with 5% CO₂. Cell numbers and viabilities were automatically measured using trypan blue dye exclusion with a Vi-Cell XR Cell Viability Analyzer (Beckman Coulter, Inc., Brea, CA, USA), according to the manufacturer's protocol.

2.4. Real-Time PCR

Relative levels of mRNA were quantified with the StepOnePlus Real-Time Polymerase Chain Reaction System (Thermo Fisher Scientific, Waltham, MA, USA) using TaqMan Fast Virus 1-Step Master Mix (Thermo Fisher Scientific) and TaqMan Gene Expression Assays (assay #Hs01076090_m1 for EGFR, assay #Hs01001580_m1 for HER2, and assay #Hs99999901_s1 for the 18S ribosomal gene as the internal control; Thermo Fisher Scientific) according to the manufacturer's protocols.

2.5. Three-Dimensional Cell Analysis

Images were captured using the FLUOVIEW™ FV3000 confocal laser scanning microscope (Olympus, Tokyo, Japan). All imaging data were analyzed with the NoviSight™ 3D cell analysis system (Olympus). Immunofluorescence staining of F-PDOs was performed using an anti-Ki-67 antibody (1:250 dilution) and 40,6-diamidino-2-phenylindole (DAPI) after fixation in phosphate buffer solution containing 4% paraformaldehyde (PFA; Fujifilm Wako Pure Chemical, Ltd.) and 1% Triton X-100 (Fujifilm Wako Pure Chemical, Ltd.). The F-PDOs were then incubated for 5 h at room temperature in AbScale solution, comprised of Dulbecco's phosphate-buffered saline (D-PBS (-); Fujifilm Wako Pure Chemical, Ltd.) containing 0.33 M urea and 0.1–0.5% Triton X-100 (30), to wash the cells. Next, the F-PDOs were incubated for 30 min at room temperature in AbScale rinse solution, comprised of 0.1x D-PBS (-) containing 2.5% BSA and 0.05% (w/v) Tween-20 (30). The rinse solution was exchanged with 4% PFA, and the F-PDOs were incubated at room temperature for 30 min.

Cetuximab and trastuzumab were labeled using the HiLyte Fluor 555 Labeling Kit-NH₂ (Dojindo Laboratories, Kumamoto, Japan) and used to quantify the cellular expression levels of EGFR and HER2. In detail, F-PDOs were incubated for 3 h with 10 µg/mL fluorophore-labeled antibodies in 24-well, flat-bottomed, ultra-low-attachment microplates (Corning, Inc.). Cells were then washed with D-PBS (-) and fixed overnight at 4 °C (39.2 °F) in 4% PFA. Subsequently, the F-PDOs were washed twice with D-PBS (-) and imbedded with 7.5% acrylamide gel. The F-PDOs were washed with D-PBS (-) and stained overnight at 4 °C (39.2 °F) with DAPI. Finally, the F-PDOs were incubated overnight at room temperature in SCALEVIEW-S4 (Fujifilm Wako Pure Chemical, Ltd.).



FLUOVIEW FV3000 System Benefits

Featuring the high sensitivity and speed required for live cell imaging as well as deep tissue observation, the FV3000 confocal microscope enables a wide range of imaging modalities, including macro-to-micro imaging, super resolution microscopy, and quantitative data analysis.

- 1 Using proprietary spectral detection technology, the FV3000 confocal microscope's TruSpectral detectors combine high sensitivity with spectral flexibility to detect even the dimmest fluorophores.
- 2 The FV3000 microscope's macro-to-micro workflow provides a roadmap for data acquisition, enabling you to see data in context and easily locate regions of interest for higher resolution imaging.
- 3 The FV3000 Hybrid Scanner provides two scanners in one for enhanced confocal imaging capabilities.
- 4 Olympus' TruFocus unit helps maintain focus during live cell imaging despite changes in temperature or added reagents.

To determine whether the effector cells could access the F-PDOs via trastuzumab, F-PDOs were treated with antibodies and then co-cultured with THP-1 effector cells that were pre-stimulated with IFN- γ . Twenty-four hours before treating F-PDOs with antibodies, IFN- (10 ng/mL) was added to the THP-1 cells, and the F-PDOs were seeded in 24-well plates, as described above. On the following day, the F-PDOs were treated with 10 or 100 $\mu\text{g/mL}$ of HiLyte Fluor 555-labeled antibodies for 30 min. Next, the THP-1 cells were rinsed with medium to wash away the IFN- γ and stained using the Cell Explore Fixable Live Cell Tracking Kit Green Fluorescence (AAT Bioquest, Inc., Sunnyvale, CA, USA). The fluorescently labelled THP-1 cells were added to the F-PDO target cells at a density of 1×10^5 cells per well and co-cultured for 3 or 120 h. The cells were fixed overnight with 4% PFA at 4 °C (39.2 °F), washed three times with D-PBS (-), imbedded with 7.5% acrylamide gel, and stained with DAPI in D-PBS (-) containing 0.1% Triton X-100. Finally, the F-PDOs were incubated overnight at room temperature in SCALEVIEW-S4.

2.6. Cell-Viability Assay

The cell viability of F-PDOs was assayed using a previously reported method (21). Briefly, each F-PDO was minced using a CellPet FT (JTEC Corporation, Osaka, Japan) equipped with a filter holder containing a 70 or 100 μm mesh filter. Each F-PDO suspension was diluted 20-fold and seeded into 384-well, round-bottomed, ultra-low-attachment microplates (Corning, Inc.) in 40 μL medium, using a Multidrop Combi Reagent Dispenser (Thermo Fisher Scientific, Inc.). At 24 h after seeding, the F-PDOs were treated with 0.04 μL solutions of different compounds using an Echo 555 Liquid Handler (Labcyte, Inc., San Jose, CA, USA) or 0.8 μL solutions of different antibodies using an ADS-348-8 Multistage-Dispense Station (Biotec Co., Ltd., Tokyo, Japan). The cells were treated with compounds or antibodies at final concentrations ranging from 1.0 nM to 20 μM or 0.195 to 100 $\mu\text{g/mL}$, respectively, using a series of 10 concentrations (serially diluted 3-fold) in each case. After 144 h, 10 μL CellTiter-Glo 3D solution (Promega Corporation, Madison, WI, USA) was added to F-PDOs in each well, and the plates were mixed using a mixer and incubated for 15 min at 25 °C (77 °F). Luminescence was measured using an EnSpire Plate Reader (PerkinElmer, Inc., Waltham, MA, USA). Cell viability was calculated by dividing the amount of ATP in the test wells by that in the vehicle-control wells, after subtracting the background levels. The growth rate over 6 days was calculated by dividing the amount of ATP in the wells without anticancer agents by those in the vehicle-control wells 24 h after seeding.

The half-maximal inhibitory concentration (IC_{50}) and area under the activity curve measuring dose response (AUC) values (used to measure dose–response relationships) were calculated from the dose–response curves and analyzed using Morphit software, version 6.0 (The Edge Software Consultancy, Ltd., Guildford, UK). As the first approach, the response curves were fitted to the luminescence signal intensities using a 4-parameter sigmoid model. Alternatively, a sigmoidal fixed-slope model without a Hill equation was used. The data shown represent the mean \pm standard deviation of triplicate experiments. The Z' factor, a dimensionless parameter that ranges between 1 (infinite separation) and < 0 , was defined as $Z' = 1 - (3\sigma^+ + 3\sigma^-)/|\mu^+ - \mu^-|$, where σ^+ , σ^- , μ^+ , and μ^- are the standard deviations (σ) and averages (μ) of the high (c^+) and low (c^-) controls (31).

2.7. Lactate Dehydrogenase (LDH) Assay

One day before cell seeding, 96-well microplates (Sumitomo Bakelite Co., Ltd., Tokyo, Japan) were coated with 50 μ L fibronectin (50 μ g/mL), and THP-1 cells were stimulated by adding 10 ng/mL IFN- γ . Each F-PDO was minced using the CellPet FT. Each F-PDO suspension was diluted 10-fold, and a 100 μ L volume of each suspension was seeded into the pre-coated plates. At 24 h after seeding the F-PDOs, 60 μ L of growth medium was removed and 10 μ L of antibody solution was added at a final concentration of 10 or 100 μ g/mL. THP-1 effector cells were added to each F-PDO at 2×10^4 cells/well 30 min after adding the antibody. Each well contained a final volume of 100 μ L. After 3 or 120 h, 25 μ L of supernatant was recovered, mixed with 25 μ L of reagent solution from the Cytotoxicity Detection KitPLUS (Roche Diagnostics, Rotkreuz, Switzerland), and incubated for 15 min. Stop solution (12.5 μ L) was added to the reaction mixture and mixed using a mixer for 10 s. Absorbance was measured at 490 and 690 nm using an EnSpire Plate Reader. Cytotoxicity was calculated by dividing the LDH activity in the test wells by that in the vehicle-control wells, after subtracting the background absorbance levels, expressed as a percentage.

2.8. Real-Time Potency Assessment Using the xCELLigence RCTA System

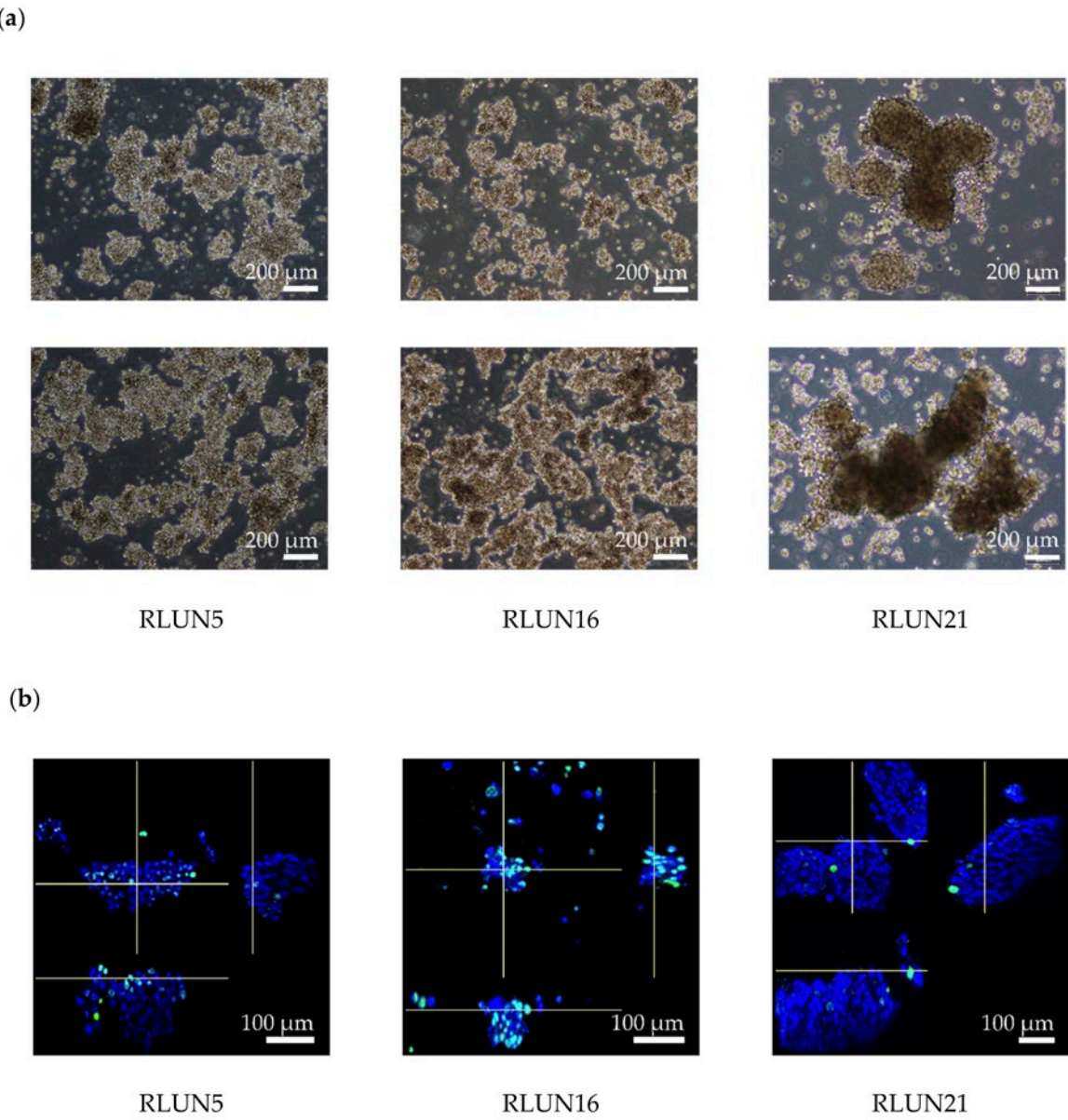
The xCELLigence RTCA System (ACEA Bioscience, San Diego, CA, USA) was used for evaluating the immune-checkpoint inhibitors. The E-plate 96 (ACEA Bioscience), which is a single-use 96-well plate specialized for performing cell-based assays with the xCELLigence RTCA System, was coated overnight with fibronectin (0.5 μ g/well) at 4 °C (39.2 °F). After removing the fibronectin, 50 μ L of culturing medium was added to each well of the E-plate to measure the background impedance. Then, each F-PDO was minced using the CellPet FT. The F-PDO suspension was diluted 15-fold, and 50 μ L of each cell suspension was seeded into the wells. The plate was placed in a safety cabinet at room temperature for 30 min and transferred to the xCELLigence RTCA instrument at 37 °C (98.6 °F) in a CO₂ incubator. At 24 h after seeding the F-PDOs into the E-plate, 60 μ L of culture media was removed from each well, and 10 μ L of antibody solution was added. PBMC were stimulated with 5 ng/mL SEB for 24 h and then added to F-PDOs 30 min post-antibody treatment. PBMCs were added at 1×10^4 cells per well to each F-PDO. Each well contained a final volume of 100 μ L. The impedance was measured every 15 min. Changes in impedance signals were measured as the cell index and then converted to percent-cytolysis values using xCELLigence immunotherapy software (ACEA Bioscience). “Percent cytolysis” refers to the percentage of target cells that were killed by effector cells, checkpoint inhibitors, or both when compared to RLUN16 cells alone (as a control). The cell indexes of wells containing PBMCs alone was subtracted from the cell indexes of the sample wells, for each time point. Next, each value was normalized to the cell index at the time just before antibody addition. The normalized cell index was converted to % cytolysis using xCELLigence immunotherapy software according to the following equation: % cytolysis = $(1 - \text{normalized cell index [sample wells]}) / \text{normalized cell index (target alone wells)} \times 100$.

3. Results and Discussion

3.1. Lung F-PDOs

The RLUN5, RLUN16, and RLUN21 lines, established from lung cancer tissues, were used in this study. RLUN5 was derived from lung cancer tissue, which was pathologically diagnosed as adenosquamous carcinoma mixed with squamous cell carcinoma and solid adenocarcinoma. RLUN16 and RLUN21 were derived from squamous cell carcinoma specimens.

RLUN5 was observed to be a mixture of cells with different morphological features (Figure 1a). The majority of RLUN5 cells appeared as cell clusters that were ~100–300 μm in diameter. RLUN16 was comprised primarily of round single cells after passaging that formed big sheets ranging from 200 to >1000 μm in diameter (Figure 1a, lower panel). The sheets were easily disrupted by pipetting or shaking (Figure 1a, upper panel). RLUN21 grew as large, firm, high-density cell clusters of 300–1000 μm in diameter that frequently merged to form clusters that were >1000 μm in diameter (Figure 1a). The doubling times of RLUN5, RLUN 16, and RLUN 21 were 5, 7, and 10 days, respectively.



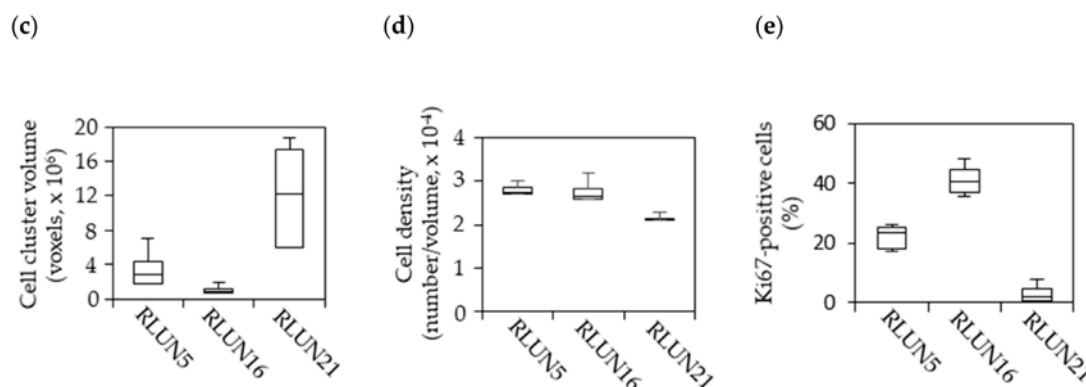


Figure 1. Phase-contrast and confocal images of three lung F-PDOs. (a) Phase-contrast images of RLUN5, RLUN16, and RLUN21 were obtained using a 4x objective. Scale bar: 200 μ m. The upper panels show each F-PDO immediately after passage, and the lower panels show each F-PDO before passage. (b) Confocal images of RLUN5, RLUN16, and RLUN21 were obtained using a 10x objective. Scale bar: 100 μ m. Ki67-expression images for RLUN5, RLUN16, and RLUN21, prepared using an anti-Ki67 antibody (green). DNA stained with DAPI (blue). (c–e) Confocal imaging data analyzed with NoviSight. (c) Box-and-whisker plot of the cell cluster volumes. (d) Box-and-whisker plot of the cell density expressed as the cell number/cell volume in a cell cluster. (e) Box-and-whisker plot of the Ki67-positive ratio expressed as 100 \times the number of positive cells/the number of total cells in a cluster.

The cell number, cell volume, cell density, and Ki67-positive cell number in four representative cell clusters of each F-PDO were analyzed with NoviSight software (Figure 1b–e). The total cell number in each cell cluster was calculated by counting the number of nuclei stained with DAPI. The median volume of RLUN21 cell clusters was larger (12×10^6 voxels) than those of RLUN5 (2.8×10^6 voxels) and RLUN 16 (0.8×10^6 voxels) (Figure 1b,c). RLUN16 clusters were very small because the big sheets readily dissociated during the experiments. The cell densities of RLUN5 and RLUN16 were almost identical (approximately 3×10^{-4} /voxel), whereas that for RLUN21 was approximately 2×10^{-4} /voxel (Figure 1d). Thus, the cell density of RLUN21 was lower than that of RLUN5 and RLUN16. Next, proliferating cells were identified by detecting Ki67, a cellular marker of proliferation. The numbers and percentages of Ki67-positive cells in cell clusters were analyzed (Figure 1b,e). Ki67-positive cells were located on the surfaces of the cell clusters, indicating that cell proliferation occurred primarily on the surface of each cell cluster. The percentages of Ki67-positive cells varied among the three F-PDOs. The ratio of Ki67-positive cells was highest for RLUN16, at approximately 40%. The ratio for RLUN21, which proliferated very slowly, was very low (2%). The characteristic structure of RLUN21 is shown in a three-dimensional (3D) video (Video S1). By performing 3D cell analysis with NoviSight software, it was possible to accurately investigate the structural features of F-PDOs possessing various structures, unlike conventional 2D analysis.

To evaluate the pharmacological activity of drugs targeting EGFR and HER2 with lung F-PDOs, the gene-expression levels of EGFR and HER2 in RLUN5, RLUN16, and RLUN21 were examined. The mRNA expression level of EGFR in RLUN21 was approximately 400-fold higher than those of RLUN5 and RLUN16 (Figure 2a). However, no difference was observed in the HER2 gene-expression levels among the three lung F-PDOs (Figure 2b).

The protein-expression levels of EGFR and HER2 in the three lung F-PDOs were detected by immunofluorescence using the monoclonal anti-EGFR antibody cetuximab and the monoclonal anti-HER2 antibody trastuzumab. The mean red-fluorescence intensity (corresponding to EGFR expression) in RLUN21 was much higher than those in RLUN5 and RLUN16, consistent with mRNA-expression analysis, and the entire surfaces of the cell clusters were strongly stained (Figure 2c). Approximately half of the cells in RLUN21 clusters were EGFR-positive (Figure 2e). Next, we confirmed the expression of the HER2 protein in these F-PDOs. The percentage of HER2-positive cells (red fluorescence) in RLUN21 clusters (65%) was >6 times that in the RLUN5 (11%) and RLUN16 (3%) clusters. The results were not identical to those for HER2 mRNA expression. HER2 was also expressed heterologously on the surface of the F-PDO clusters. Heterologous expression of HER2 is a feature of F-PDO, which is an important insight gained from 3D cell analysis.

We examined whether EGF, a ligand for EGFR, affected RLUN21 proliferation because RLUN21 showed high EGFR expression. The F-PDOs were cultured in medium with or without EGF for six days. The cell-growth rate was calculated by measuring the ATP contents to count viable cells. As expected, RLUN21 proliferation increased 2.6-fold in medium with EGF and, thus, was dependent on EGF (Figure 3a,b). However, RLUN5 and RLUN16 proliferation did not change after EGF was added to the culture medium. Next, the number of Ki67-positive cells in RLUN21 cell clusters was analyzed by immunofluorescence (Figure 3c). The positive-cell ratios in RLUN21 cell clusters cultured with EGF were two-fold higher than those in culture without EGF (Figure 3d). In addition, the cell clusters cultured with EGF showed a lower cell density and were loose (Figure 3e). These results suggest EGF induced RLUN21 cell division by activating the EGFR signal pathway.

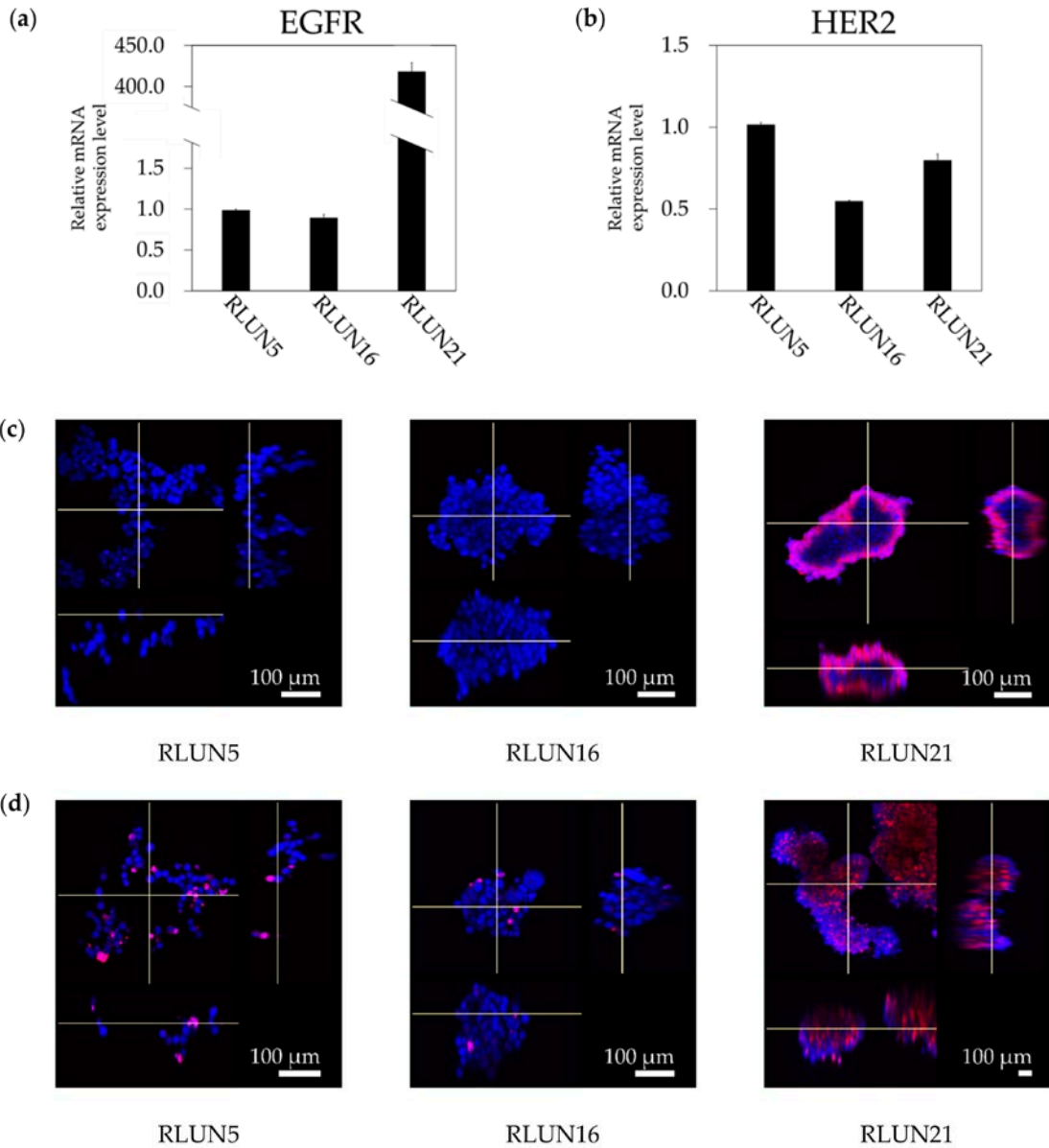


Figure 2. Expression of epidermal growth factor receptor (EGFR) and human epidermal growth factor receptor 2 (HER2) in three lung F-PDOs. mRNA-expression levels of (a) EGFR and (b) HER2 in RLUN5, RLUN16, and RLUN21. Gene-expression levels were normalized against that of 18S rRNA gene, using the $2^{-\Delta\Delta Ct}$ method. The expression data for RLUN16 and RLUN21 were normalized to those for RLUN5, which was set to 1. The error bars indicate the standard deviation from three replicate samples. (c) EGFR-expression images of RLUN5, RLUN16, and RLUN21 stained with fluorescently labeled cetuximab (red). (d) HER2-expression images stained with fluorescently labeled trastuzumab (red). DNA stained with DAPI (blue). Magnification: 10x. Scale bar: 100 μm. Box-and-whisker plots of the ratio of cells positive for EGFR (e) or HER2 (f), calculated as 100× volume of positive cells/volume of cells in a cluster.

Taken together, these data indicate that F-PDOs displayed various distinct structural and biological characteristics when compared to conventional cell lines cultured in monolayers.

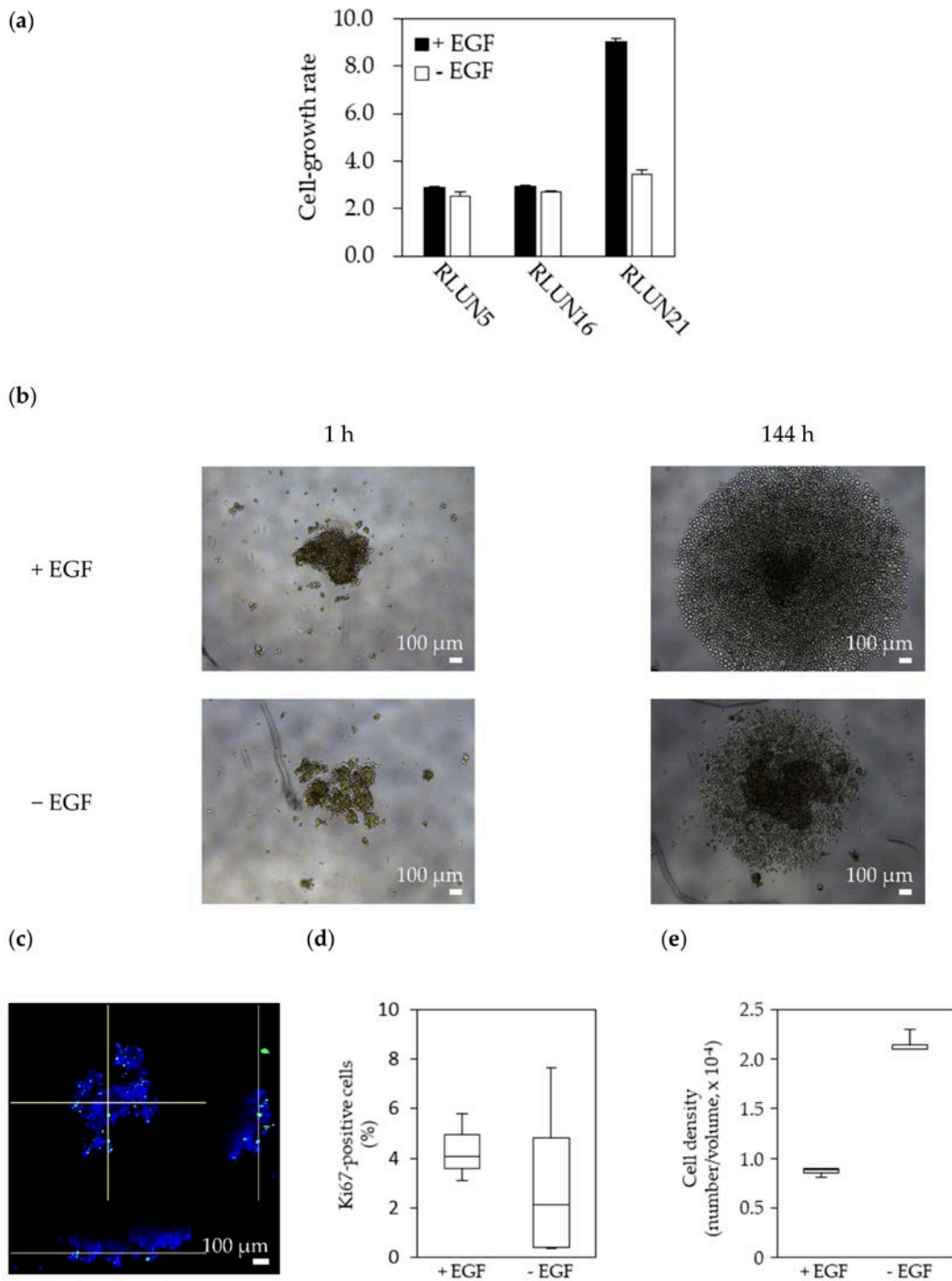


Figure 3. Dependency of F-PDO proliferation on epidermal growth factor (EGF). (a) Growth rate of RLUN5, RLUN16, and RLUN21 in the presence or absence of EGF. Each F-PDO was seeded in a 96-well, round-bottomed, ultra-low-attachment microplate (Corning, Inc.). Twenty-four hours after seeding, EGF was added into the wells at a final concentration of 100 ng/mL. The wells without EGF were also set up to confirm the dependency of cell growth on EGF. One hour (culture start time) or 144 h later, the amount of ATP was measured as described in Section 2.6. Growth rates were calculated by dividing the amount of ATP in each well at 144 h by that at the culture start time. (b) Phase-contrast images of RLUN21 cultured with EGF (upper panels) or without EGF (lower panels) for six days. The images were obtained using a 5X objective. Scale bar: 100 μ m. (c) Images of Ki67 expression in RLUN21 cultured with EGF were obtained using an anti-Ki67 antibody (green). DNA stained with DAPI (blue). Magnification: 10x. Scale bar: 100 μ m. Box-and-whisker plot of the Ki67-positive ratio (d) and cell density (e) of RLUN21 cells cultured with EGF.

3.2. Evaluation of Small-Molecule Drugs Using F-PDOs

To determine the sensitivity of the lung F-PDOs to anticancer agents, including EGFR and HER2 inhibitors, using our HTS system with 384-well plates, growth inhibition was assessed using RLUN5, RLUN 16, and RLUN 21. EGFR inhibitors are used as standard clinical treatments for lung cancer. F-PDOs were treated with EGFR inhibitors 24 h post-seeding and were subsequently incubated for six days. The ATP contents were measured to count the viable cells. The HTS performance was evaluated by computing the Z0 factor. The Z0 factor has been widely accepted as a means for evaluating assay quality and performance, and an assay is considered suitable for HTS when the Z0 factor value is >0.5 (31). The F-PDOs showed 2.7–5.8 fold growth in the plates. The control data points in the 384-well plate assay had calculated Z0 factor values of 0.63, 0.94, and 0.62 for RLUN5, RLUN16, and RLUN21, respectively. These results suggested that this assay performed well for HTS, using 384-well plates to evaluate anticancer agents.

The half-maximal inhibitory concentration (IC50) and area under the activity curve measuring dose response (AUC) values of anticancer agents observed with each F-PDO are presented in Figure 4 and Tables S2–S4. AUC values do not require extrapolation and can be estimated from dose-response curves. Therefore, AUC values are often used to evaluate the efficacies of anticancer agents. The AUC values demonstrated that three F-PDOs were similarly sensitive to anti-cancer drugs. RLUN21, which is dependent on EGFR signaling pathway, was more sensitive to inhibitors targeting members of the EGFR signaling pathway than other F-PDOs (Figure 4a). In particular, RLUN21 proliferation was slowed more by the inhibitors when cultured with EGF than without EGF (Figure 4a). These results confirmed that RLUN21 proliferation was highly dependent on the EGFR pathway.

RLUN5 showed higher sensitivity to chemotherapeutic agents than other F-PDOs, whereas RLUN21 showed resistance to chemotherapeutic agents (Figure 4c). In particular, the microtubuletargeting cytotoxic agents, paclitaxel, and vindesine, did not significantly inhibit the proliferation of RLUN21, which proliferated very slowly and did not possess Ki67-positive cells (Figure 1b,e). However, RLUN21 clusters were more sensitive to microtubule-targeting cytotoxic agents in the presence of EGF than in the absence of EGF. These results imply that antimitotic agents strongly act on actively dividing cells.

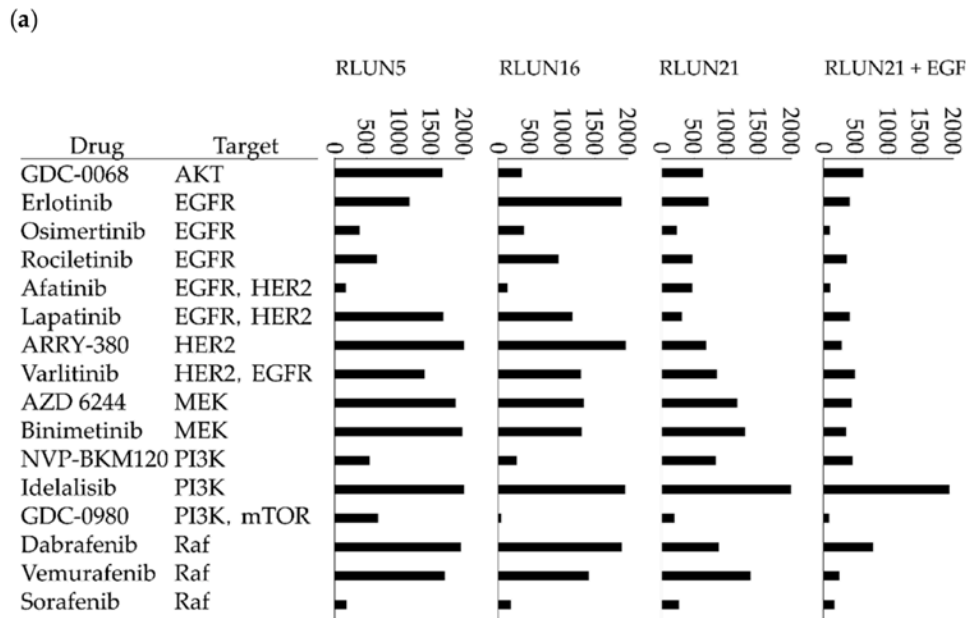


Figure 4. Cont.

(b)

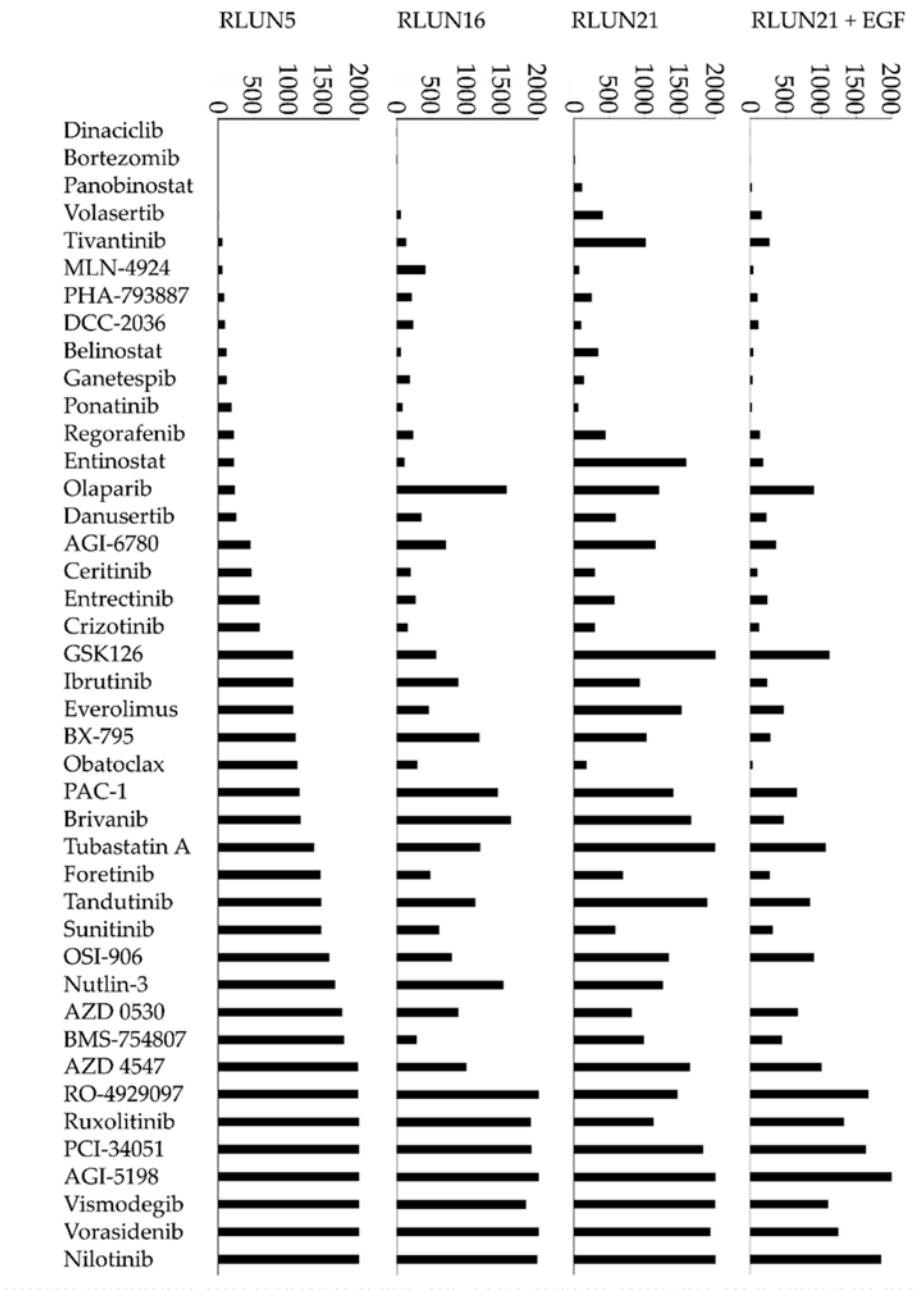


Figure 4. Cont.

(c)

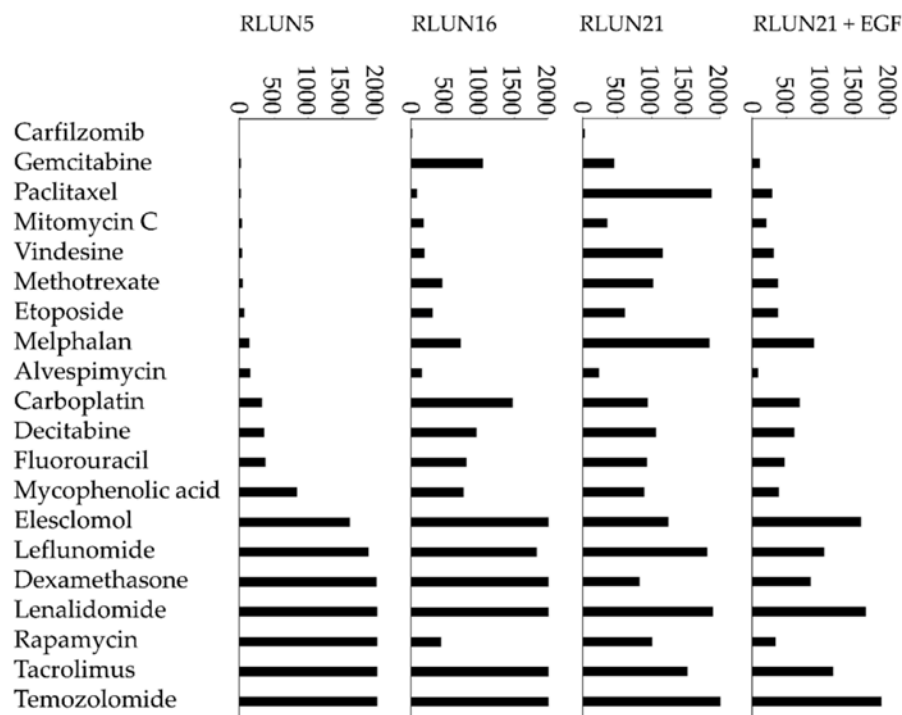


Figure 4. Response of F-PDOs to anti-cancer agents. The bar graphs represent the area under the activity curve measuring dose response (AUC) values calculated from the growth-inhibition assays, using 78 anticancer agents at concentrations ranging from 3 nM to 20 μ M. The AUC values show the area under each fitting curve calculated from each dose-response curve. The AUC value of a sample not treated with an anti-cancer drug was 2000. Low AUC values indicate cases where F-PDOs were more sensitive to an anti-cancer drug. Values above 2000 indicate cases where the cells grew more than the untreated sample. The data shown represent the mean of triplicate experiments. The column entitled “RLUN21 + EGF” indicates cases where the F-PDOs were grown in the presence of EGF. (a) Molecular target drugs that inhibit the EGFR signal pathway. (b) Other molecular target drugs. (c) Chemotherapeutic drugs.

The F-PDO donors had no history of EGFR inhibitor administration. Therefore, the effects of EGFR inhibitors against PDOs could not be compared to assess the clinical efficacies. However, the donor of RLUN16 was previously administered cisplatin and vinorelbine (a microtubule-targeting agent) after surgery, and had no recurrence of cancer. RLUN16 showed high sensitivity to paclitaxel and vindesine. Thus, the results suggest that the evaluation of anticancer drug using F-PDO reflects the clinical efficacy. Overall, these results demonstrated the suitability of the HTS system for evaluating various anticancer agents, including molecular targeted and chemotherapeutic drugs against lung F-PDOs in 384-well plate format.

3.3. Evaluation of Antibody Drugs Using F-PDOs

3.3.1. Evaluation of Monoclonal Antibodies and an ADC

Growth inhibition was assessed using the HTS system with 384-well plates to investigate the sensitivity of three F-PDOs to monoclonal antibody drugs for cancer. To this end, we tested cetuximab (which targets EGFR); trastuzumab (which targets HER2); pertuzumab (which inhibits the dimerization of HER2 with other HER homologs); and trastuzumab emtansine (which is an ADC consisting of trastuzumab covalently linked to the microtubule-targeting cytotoxic agent DM1 that targets HER2). F-PDOs were treated with the indicated drugs 24 h post-seeding and were subsequently incubated for six days. The viable F-PDO cells were counted. Cetuximab inhibited the proliferation of RLUN21 in a dose-dependent manner with an IC_{50} value of 2.4 $\mu\text{g/mL}$, whereas the IC_{50} values were $>100 \mu\text{g/mL}$ for RLUN5 and RLUN16, which are not dependent on EGF for proliferation (Table 1). These results suggest that inhibiting EGFR signaling in RLUN21 with cetuximab induced growth inhibition due to high EGFR expression and EGF dependency for proliferation in RLUN21.

Trastuzumab did not inhibit the growth of RLUN5, RLUN16, or RLUN21, indicating that trastuzumab could not neutralize these F-PDOs. However, the IC_{50} values of an ADC, trastuzumab emtansine, were 3.4, 4.9, and 1.7 $\mu\text{g/mL}$ for RLUN5, RLUN16, and RLUN21, respectively, and the ADC showed strong cytotoxic effects against each F-PDO. The values were weakly correlated with the protein-expression level of HER2 (Figure 2f). Even RLUN16 with weak HER2 expression (2.8% of the all cells were HER2-positive) showed a high effect of the ADC due to a bystander effect, wherein a cytotoxic agent released from cancer cells penetrated the cell membranes of neighboring dividing cancer cells and exerted further cytotoxic effects (32). In addition, trastuzumab emtansine, an ADC that functions as a microtubule-targeting cytotoxic agent, strongly induced cell death in RLUN21 despite the resistance of RLUN21 to microtubule-targeting cytotoxic agents (Figure 4c). These results suggest that ADCs may serve as effective cancer drugs in clinical use.

Table 1. Half-maximal inhibitory concentration (IC_{50}) values of trastuzumab, pertuzumab, cetuximab, and trastuzumab emtansine against each F-PDO.

	RLUN5	RLUN16	RLUN21
Cetuximab	>100	>100	2.4
Trastuzumab	>100	>100	>100
Pertuzumab	>100	>100	>100
Trastuzumab emtansine	3.4	4.9	1.7

IC_{50} values reflect concentrations in term of $\mu\text{g/mL}$.

3.3.2. ADCC Activity of Trastuzumab Against RLUN21

Trastuzumab did not show neutralizing activity against the F-PDOs used in this study (Table 1). To confirm this lack of ADCC activity against F-PDOs, we tested effector cell-mediated cytotoxicity with the anti-HER2 antibody trastuzumab in RLUN21 cells, which overexpressed HER2. ADCC is a defense mechanism involving cellular immunity, whereby effector cells of the immune system actively lyse cancer cells, whose membrane-surface antigens are bound by specific antibodies. To measure ADCC activities, the monocyte cell line THP-1 was used as the effector cells, and cytotoxicity was measured as the activity of extracellularly released LDH from F-PDOs when killed by THP-1 cells. The percentage of cytotoxicity was detected by measuring the LDH activity, and THP-1 cells were used as effector cells. RLUN21 cells treated with 100 $\mu\text{g/mL}$ trastuzumab showed significantly more cytotoxicity in the presence of THP-1 effector cells than in the absence of THP-1 cells at 120 h after THP-1 cell addition, although no such effect was observed with 10 $\mu\text{g/mL}$ trastuzumab or at 3 h after THP-1 addition (Figure 5a).

Next, we observed interactions between F-PDO and THP-1 effector cells via trastuzumab. At 3 h after co-culturing RLUN21 and THP-1 cells, THP-1 cells had begun to gather around the RLUN21 cell clusters via trastuzumab (Figure 5b). THP-1 cells invaded RLUN21 cell clusters treated with 100 µg/mL trastuzumab at 120 h, but RLUN21 clusters treated with 10 µg/mL trastuzumab did not show differences after 3 h. These results imply that the invasion of THP-1 cells into the cell clusters causes the cytolysis of RLUN21.

Taken together, these results revealed that these F-PDOs can be used for evaluating the efficacies of neutralizing activity, ADCC activity, and ADC.

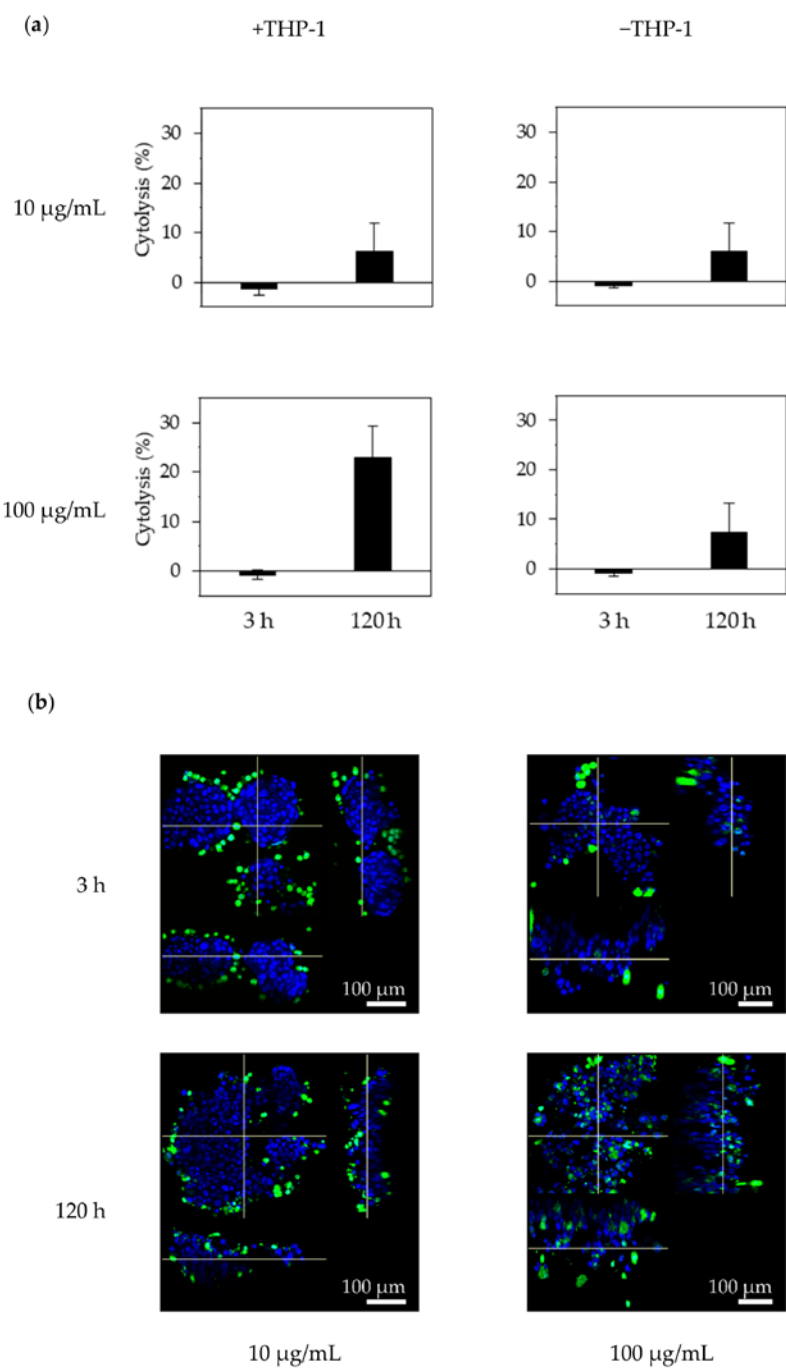


Figure 5. Antibody-dependent cellular cytotoxicity (ADCC) activity against RLUN21 cells with trastuzumab. (a) Cytolysis against RLUN21 by trastuzumab and THP-1 effector cells was determined by performing lactate Dehydrogenase (LDH) assays. Cytolysis (%) was calculated as 100 × (LDH release in test well –LDH release from RLUN21 cells only –LDH release from THP-1 cells only)/(maximum LDH release from RLUN21 cells lysed using Triton X-100 –LDH release from RLUN21 cells only). Cytolysis was measured at 3 and 120 h after THP-1 addition. The error bars indicate the standard deviation from six replicate samples. (b) Interaction of THP-1 effector cells with RLUN21 cell during ADCC. Magnification: ×30. Scale bar: 100 µm. THP-1 cells stained using the Cell Explore Fixable Live Cell Tracking Kit are shown in green. DNA stained with DAPI is shown in blue.

3.4. Evaluation of Immune-Checkpoint Inhibitors Using F-PDOs

We performed experiments using RLUN16 and PBMCs, respectively, as target and effector cells, as well as nivolumab and pembrolizumab, which are monoclonal antibodies targeting PD-1 as immune checkpoint inhibitors. We selected the xCELLigence platform, which can be used to monitor the number, morphology, and attachment of cells for a long duration. To induce the adequate expression of PD-1 in PBMCs for the immune-checkpoint experiments, the effector cells were treated with the bacterial superantigen SEB (5 ng/mL) beginning at one day before adding the target cells and were continuously stimulated throughout the measurements. RLUN16 cells were treated with SEB-stimulated PBMCs in the presence of nivolumab and pembrolizumab. As shown in Figure 6, SEB-stimulated PBMCs reduced RLUN16 cell proliferation by only 20%, compared with control cells. The percent cytolysis of RLUN16 cells following treatment with nivolumab (Figure 6a) or pembrolizumab (Figure 6b) alone was almost identical to that after co-culture with PBMCs. In contrast, the presence of nivolumab and pembrolizumab led to a significant increase in PBMC-mediated RLUN16 cell killing. The cytolytic activity in the presence of 1 $\mu\text{g/mL}$ pembrolizumab was greater than that observed in the presence of 50 $\mu\text{g/mL}$ nivolumab. This result may reflect differences in the binding affinities of pembrolizumab and nivolumab to PD-1 (33). The K_d value (i.e., the equilibrium dissociation constant between the antibody and its antigen) of pembrolizumab is 0.028 nM, while nivolumab is 2.6 nM (33). Thus, a 100-fold difference in the K_d values was consistent with the biological evaluations using F-PDOs. In summary, these results demonstrate that the F-PDO assay system with real-time, impedance-based technology can be utilized for assessing immune-checkpoint inhibitors.

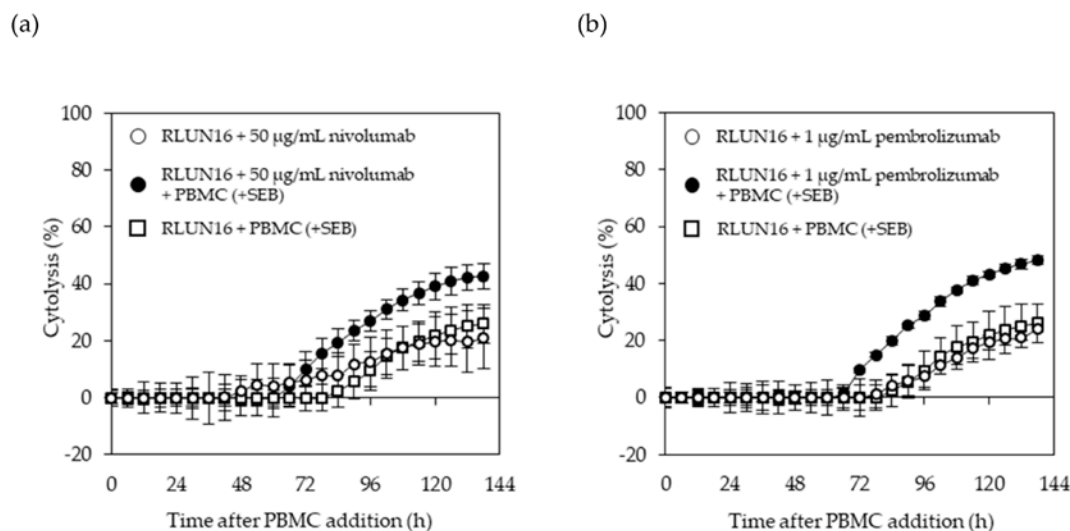


Figure 6. Impedance measurements of RLUN16 cell cytolysis by nivolumab (a) or pembrolizumab (b). Open circles, anti-PD-1 antibody alone; closed circles, anti-PD-1 antibody in combination with Staphylococcal enterotoxin B (SEB)-stimulated peripheral blood mononuclear cells (PBMCs); open squares, SEB-stimulated PBMCs alone. Nivolumab and pembrolizumab were used at concentrations of 50 and 1 $\mu\text{g/mL}$, respectively. Dynamic changes in the cell-index values were recorded over time.

4. Conclusions

In conclusion, we developed systems for assaying molecular target drugs, antibody drugs, ACDs, and immune-checkpoint inhibitors using F-PDOs, which are characteristically similar to the source tissues. In addition, our results indicated that F-PDOs have structural characteristics enabling the construction of an evaluation system for anticancer drugs, based on structural changes of F-PDO found with a 3D cell-analysis system, demonstrating that 3D cell analysis is a powerful tool for analyzing the characteristics of PDOs. Finally, the results of this study demonstrate that F-PDOs with various distinct structural and biological characteristics are superior for identifying potential novel molecular target drugs for cancer.

Supplementary Materials: The following are available online at <http://www.mdpi.com/2073-4409/8/5/481/s1>, Table S1: anticancer agents used in the present study, Video S1: video of a cell cluster of RLUN21.

Author Contributions: Conceptualization, M.T.; funding acquisition, S.W.; investigation, N.T., H.H, A.H., G.H., H.T., M.O, K.T., and K.G.; methodology, H.H, A.H., G.H., H.T., M.O, K.T., K.G., and M.T.; resources, H.T., N.O., S.M., and H.S.; supervision, K.S. and S.W.; validation, H.H and M.T.; writing—original draft, N.T., H.H., A.H., and M.T.; writing—review and editing, M.T.

Funding: Translational Research Programs from Fukushima Prefecture.

Acknowledgments: We thank the staff of the Translational Research Center.

Conflicts of Interest: The authors declare no conflict of interest. The funders had no role in the design of the study; in the collection, analyses, or interpretation of data; in the writing of the manuscript, or in the decision to publish the results.

Authors

This paper has been published by Takahashi, N.; Hoshi, H.; Higa, A.; Hiya, G.; Tamura, H.; Ogawa, M.; Takagi, K.; Goda, K.; Okabe, N.; Muto, S.; Suzuki, H.; Shimomura, K.; Watanabe, S.; Takagi, M. in the following journal: *Cells* 2019, 8, 481. The original paper is licensed under the CC BY 4.0 license. Olympus added a foreword and adapted the paper to its corporate design. None of these adaptations shall indicate that the authors endorse Olympus or this adapted publication. The original paper is available at <https://www.mdpi.com/2073-4409/8/5/481>.

References

1. Baudino, T.A. Targeted cancer therapy: The next generation of cancer treatment. *Curr. Drug Discov. Technol.* 2015, 12, 3–20. [CrossRef]
2. Kumar, B.; Singh, S.; Skvortsova, I.; Kumar, V. Promising targets in anti-cancer drug development: Recent updates. *Curr. Med. Chem.* 2017, 24, 4729–4752. [CrossRef]
3. Ke, X.; Shen, L. Molecular targeted therapy of cancer: The progress and future prospect. *Front. Lab. Med.* 2017, 1, 69–75. [CrossRef]
4. Sharma, S.V.; Haber, D.A.; Settleman, J. Cell line-based platforms to evaluate the therapeutic efficacy of candidate anticancer agents. *Nat. Rev. Cancer* 2010, 10, 241–253. [CrossRef] [PubMed]
5. Shamir, E.R.; Ewald, A.J. Three-dimensional organotypic culture: Experimental models of mammalian biology and disease. *Nat. Rev. Mol. Cell Biol.* 2014, 15, 647–664. [CrossRef]
6. Arrowsmith, J.; Miller, P. Trial watch: Phase II and phase III attrition rates 2011–2012. *Nat. Rev. Drug Discov.* 2013, 12, 569. [CrossRef] [PubMed]
7. Arrowsmith, J. Trial watch: Phase II failures 2008–2010. *Nat. Rev. Drug Discov.* 2011, 10, 328–329. [CrossRef]
8. DiMasi, J.A.; Reichert, J.M.; Feldman, L.; Malins, A. Clinical approval success rates for investigational cancer drugs. *Clin. Pharmacol. Ther.* 2013, 94, 329–335. [CrossRef]
9. Crespo, M.; Vilar, E.; Tsai, S.Y.; Chang, K.; Amin, S.; Srinivasan, T.; Zhang, T.; Pipalia, N.H.; Chen, H.J.; Witherspoon, M.; et al. Colonic organoids derived from human induced pluripotent stem cells for modeling colorectal cancer and drug testing. *Nat. Med.* 2017, 23, 878–884. [CrossRef] [PubMed]
10. Sato, T.; Stange, D.E.; Ferrante, M.; Vries, R.G.; Van Es, J.H.; Van den Brink, S.; Van Houdt, W.J.; Pronk, A.; Van Gorp, J.; Siersema, P.D.; et al. Long-term expansion of epithelial organoids from human colon, adenoma, adenocarcinoma, and Barrett's epithelium. *Gastroenterology* 2011, 141, 1762–1772. [CrossRef] [PubMed]
11. Van de Wetering, M.; Francies, H.E.; Francis, J.M.; Bounova, G.; Iorio, F.; Pronk, A.; Van Houdt, W.; Van Gorp, J.; Taylor-Weiner, A.; Kester, L.; et al. Prospective derivation of a living organoid biobank of colorectal cancer patients. *Cell* 2015, 161, 933–945. [CrossRef] [PubMed]
12. Boj, S.F.; Hwang, C.I.; Baker, L.A.; Chio, I.I.; Engle, D.D.; Corbo, V.; Jager, M.; Ponz-Sarvisé, M.; Tiriác, H.; Spector, M.S.; et al. Organoid models of human and mouse ductal pancreatic cancer. *Cell* 2015, 160, 324–338. [CrossRef] [PubMed]
13. Gao, D.; Vela, I.; Sboner, A.; Iaquinta, P.J.; Karthaus, W.R.; Gopalan, A.; Dowling, C.; Wanjala, J.N.; Undvall, E.A.; Arora, V.K.; et al. Organoid cultures derived from patients with advanced prostate cancer. *Cell* 2014, 159, 176–187. [CrossRef]
14. Girda, E.; Huang, E.C.; Leiserowitz, G.S.; Smith, L.H. The use of endometrial cancer patient-derived organoid culture for drug sensitivity testing is feasible. *Int. J. Gynecol. Cancer* 2017, 27, 1701–1707. [CrossRef] [PubMed]
15. Broutier, L.; Mastrogianni, G.; Verstegen, M.M.; Francies, H.E.; Gavarró, L.M.; Bradshaw, C.R.; Allen, G.E.; Ames-Benito, R.; Sidorova, O.; Gaspersz, M.P.; et al. Human primary liver cancer-derived organoid cultures for disease modeling and drug screening. *Nat. Med.* 2017, 23, 1424–1435. [CrossRef] [PubMed]
16. Pauli, C.; Hopkins, B.D.; Prandi, D.; Shaw, R.; Fedrizzi, T.; Sboner, A.; Sailer, V.; Augello, M.; Puca, L.; Rosati, R.; et al. Personalized in vitro and in vivo cancer models to guide precision medicine. *Cancer Discov.* 2017, 7, 462–477. [CrossRef]
17. Kondo, J.; Endo, H.; Okuyama, H.; Ishikawa, O.; Iishi, H.; Tsujii, M.; Ohue, M.; Inoue, M. Retaining cell-cell contact enables preparation and culture of spheroids composed of pure primary cancer cells from colorectal cancer. *Proc. Natl. Acad. Sci. USA* 2011, 108, 6235–6240. [CrossRef]
18. Endo, H.; Okami, J.; Okuyama, H.; Kumagai, T.; Uchida, J.; Kondo, J.; Takehara, T.; Nishizawa, Y.; Imamura, F.; Higashiyama, M.; et al. Spheroid culture of primary lung cancer cells with neuregulin 1/HER3 pathway activation. *J. Thorac. Oncol.* 2013, 8, 131–139. [CrossRef] [PubMed]
19. Kiyohara, Y.; Yoshino, K.; Kubota, S.; Okuyama, H.; Endo, H.; Ueda, Y.; Kimura, T.; Kimura, T.; Kamiura, S.; Inoue, M. Drug screening and grouping by sensitivity with a panel of primary cultured cancer spheroids derived from endometrial cancer. *Cancer Sci.* 2016, 107, 452–460. [CrossRef]
20. Yoshida, T.; Okuyama, H.; Endo, H.; Inoue, M. Spheroid cultures of primary urothelial cancer cells: Cancer tissue-originated spheroid (CTOS) method. *Methods Mol. Biol.* 2018, 1655, 145–153. [CrossRef]

21. Tamura, H.; Higa, A.; Hoshi, H.; Hiyama, G.; Takahashi, N.; Ryufuku, M.; Morisawa, G.; Yanagisawa, Y.; Ito, E.; Imai, J.I.; et al. Evaluation of anticancer agents using patient-derived tumor organoids characteristically similar to source tissues. *Oncol. Rep.* 2018, 40, 635–646. [CrossRef]
22. Singh, D.; Attri, B.K.; Gill, R.K.; Bariwal, J. Review on EGFR inhibitors: Critical updates. *Mini Rev. Med. Chem.* 2016, 16, 1134–1166. [CrossRef]
23. Ai, X.; Guo, X.; Wang, J.; Stancu, A.L.; Joslin, P.M.N.; Zhang, D.; Zhu, S. Targeted therapies for advanced non-small cell lung cancer. *Oncotarget* 2018, 9, 37589–37607. [CrossRef]
24. Roskoski, R., Jr. Small molecule inhibitors targeting the EGFR/ErbB family of protein-tyrosine kinases in human cancers. *Pharmacol. Res.* 2019, 139, 395–411. [CrossRef]
25. Hoshi, H.; Hiyama, G.; Ishikawa, K.; Inageda, K.; Fujimoto, J.; Wakamatsu, A.; Togashi, T.; Kawamura, Y.; Takahashi, N.; Higa, A.; et al. Construction of a novel cell-based assay for the evaluation of anti-EGFR drug efficacy against EGFR mutation. *Oncol. Rep.* 2017, 37, 66–76. [CrossRef]
26. Waks, A.G.; Winer, E.P. Breast cancer treatment: A review. *JAMA* 2019, 321, 288–300. [CrossRef]
27. Cerignoli, F.; Abassi, Y.A.; Lamarche, B.J.; Guenther, G.; Santa Ana, D.; Guimet, D.; Zhang, W.; Zhang, J.; Xi, B. In vitro immunotherapy potency assays using real-time cell analysis. *PLoS ONE* 2018, 13, e0193498. [CrossRef] [PubMed]
28. Prasad, V.; Kaestner, V. Nivolumab and pembrolizumab: Monoclonal antibodies against programmed cell death-1 (PD-1) that are interchangeable. *Semin. Oncol.* 2017, 44, 132–135. [CrossRef]
29. Fessas, P.; Lee, H.; Ikemizu, S.; Janowitz, T. A molecular and preclinical comparison of the PD-1-targeted T-cell checkpoint inhibitors nivolumab and pembrolizumab. *Semin. Oncol.* 2017, 44, 136–140. [CrossRef] [PubMed]
30. Hama, H.; Hioki, H.; Namiki, K.; Hoshida, T.; Kurokawa, H.; Ishidate, F.; Kaneko, T.; Akagi, T.; Saito, T.; Saido, T.; et al. ScaleS: An optical clearing palette for biological imaging. *Nat. Neurosci.* 2015, 18, 1518–1529. [CrossRef] [PubMed]
31. Zhang, J.H.; Chung, T.D.; Oldenburg, K.R. A simple statistical parameter for use in evaluation and validation of high throughput screening assays. *J. Biomol. Screen.* 1999, 4, 67–73. [CrossRef]
32. Staudacher, A.H.; Brown, M.P. Antibody drug conjugates and bystander killing: Is antigen-dependent internalisation required? *Br. J. Cancer* 2017, 117, 1736–1742. [CrossRef] [PubMed]
33. Mahoney, K.M.; Freeman, G.J.; McDermott, D.F. The next immune-checkpoint inhibitors: PD-1/PD-L1 blockade in melanoma. *Clin. Ther.* 2015, 37, 764–782. [CrossRef] [PubMed]

© 2019 by the authors. Licensee MDPI, Basel, Switzerland. This article is an open access article distributed under the terms and conditions of the Creative Commons Attribution (CC BY) license (<http://creativecommons.org/licenses/by/4.0/>).

3D Analysis of Patient-Derived Tumor Organoids

Confocal images of patient-derived tumor organoids (PDOs) were quantitatively analyzed using NoviSight™ 3D software to evaluate their morphological features and antibody binding of molecular targeted drugs.

Introduction

3D tissue models are popular for drug discovery since they mimic the in vivo microenvironment. PDOs are one of the most powerful tools to recapitulate the original patients' drug response. In fact, a recent study reveals that phenotypic and genotypic profiling of PDOs feature a high degree of similarity to the original patient tumor. More importantly, the PDOs could predict drug reactivity with more than 80% accuracy.

By using Fukushima patient-derived tumor organoids (F-PDO®), Olympus' FLUOVIEW™ FV3000 confocal laser scanning microscope, and NoviSight™ 3D analysis software, we offer a novel workflow for studying PDO morphology and drug distribution.

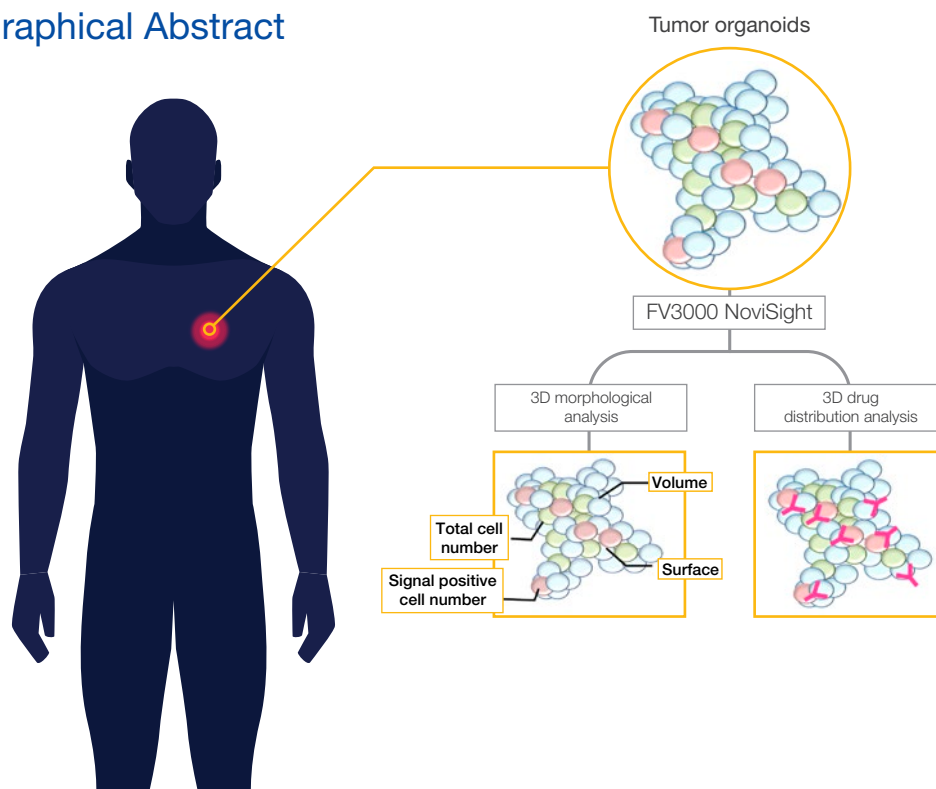


Novisight Software Benefits

Olympus' NoviSight™ software with True 3D cell analysis technology helps accelerate drug discovery research. Designed for our laser scanning confocal microscopes, NoviSight software facilitates data interpretation and validation through its practical features.

- 1 Recognition, analysis, and statistical results are displayed on one screen
- 2 Switch between 3D and 2D views with scatterplot, heat map, and graph display options. Clicking points in these display options shows the corresponding images
- 3 Export data as CSV and FCS files for further analysis

Graphical Abstract



Benefits

- Image and analyze PDOs while retaining the information in their 3D structure.
- NoviSight software can identify objects in 3D, classify the objects, and deliver statistical data.

Methods

Cell preparation

To prepare the cells, we used three types of lung F-PDOs (RLUN5, RLUN16, and RLUN21). RLUN5 was grown from an adenosquamous carcinoma tumor while RLUN16 and RLUN21 were grown from a squamous carcinoma tumor. RLUN21 forms large cell aggregates and features a larger cytoplasm than the others (Fig. 1).

The F-PDOs were then centrifuged, collected, and fixed with 4% paraformaldehyde overnight. Erbitux®, an epidermal growth factor receptor (EGFR) inhibitor, and Herceptin®, a human epidermal growth factor receptor 2 (HER2) inhibitor, were labeled with HiLyte™ Fluor 555 (Chemical Dojin) and incubated with F-PDOs for three hours.

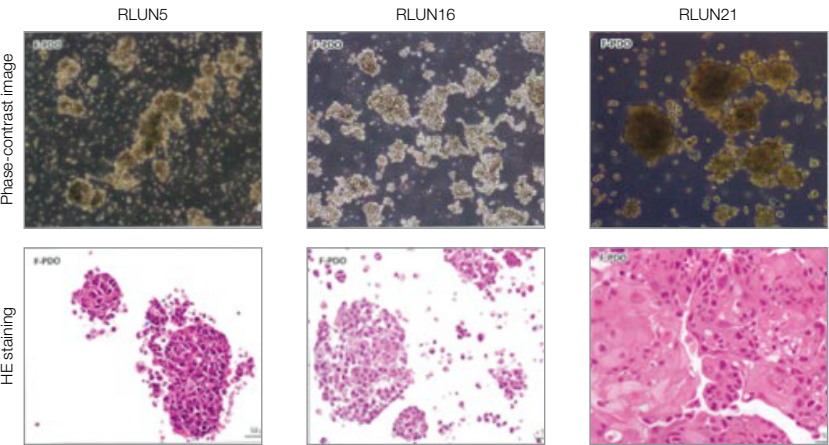


Figure 1. F-PDOs

Immunostaining and clearing

We performed the Hama et al. immunostaining protocol with some modification (Fig. 2). Each fixed F-PDO was incubated overnight with a Ki67 antibody (Abcam, 16667) and diluted with AbScale solution (0.33 M Urea and 0.2% Triton-X100). After washing with AbScale, the F-PDOs were incubated with a second antibody for three hours and diluted with AbScale. After washing with AbScale rinse solution for an hour, F-PDOs were refixed with 4% paraformaldehyde. Then they were washed with a phosphate-buffered saline (PBS) solution and incubated overnight using the clearing reagent ScaleS4 with DAPI. The cleared F-PDOs were then imaged with Olympus’ FV3000 confocal laser scanning microscope.

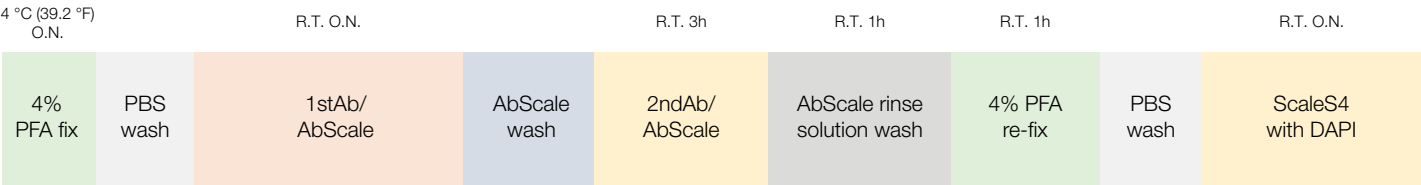


Figure 2. F-PDOs immunostaining and clearing scheme

Imaging and analysis

We used 10x or 30x magnification with 2 μm Z pitch to capture images of the cleared F-PDOs for 3D analysis. An appropriate Z pitch setting is important for accurate 3D cell analysis. The images were then imported into NoviSight™ software and reconstructed in 3D. NoviSight software can recognize 3D objects, such as a nuclei, and convert them into quantitative data.

Results

3D quantification of F-PDO morphology

NoviSight software enabled us to quantify PDOs using several Z-plane images. By staining their nuclei, the analysis software captured the whole structure and enabled single cell recognition (Fig. 3A). It also added each recognized object on the graph as a single plot. When the software recognized each nucleus as an object, we extracted Ki67 positive cells both graphically and three dimensionally by gating high Ki67 intensity plots (Fig. 3B). Using these methods, we quantified the F-PDO’s cell number, volume, cell density, and Ki67 positive cell ratio (Fig. 3C). We found RLUN21’s Ki67 positive ratio was lower than the others. Also, the larger cytoplasm RLUN21 may have caused its low cell density.

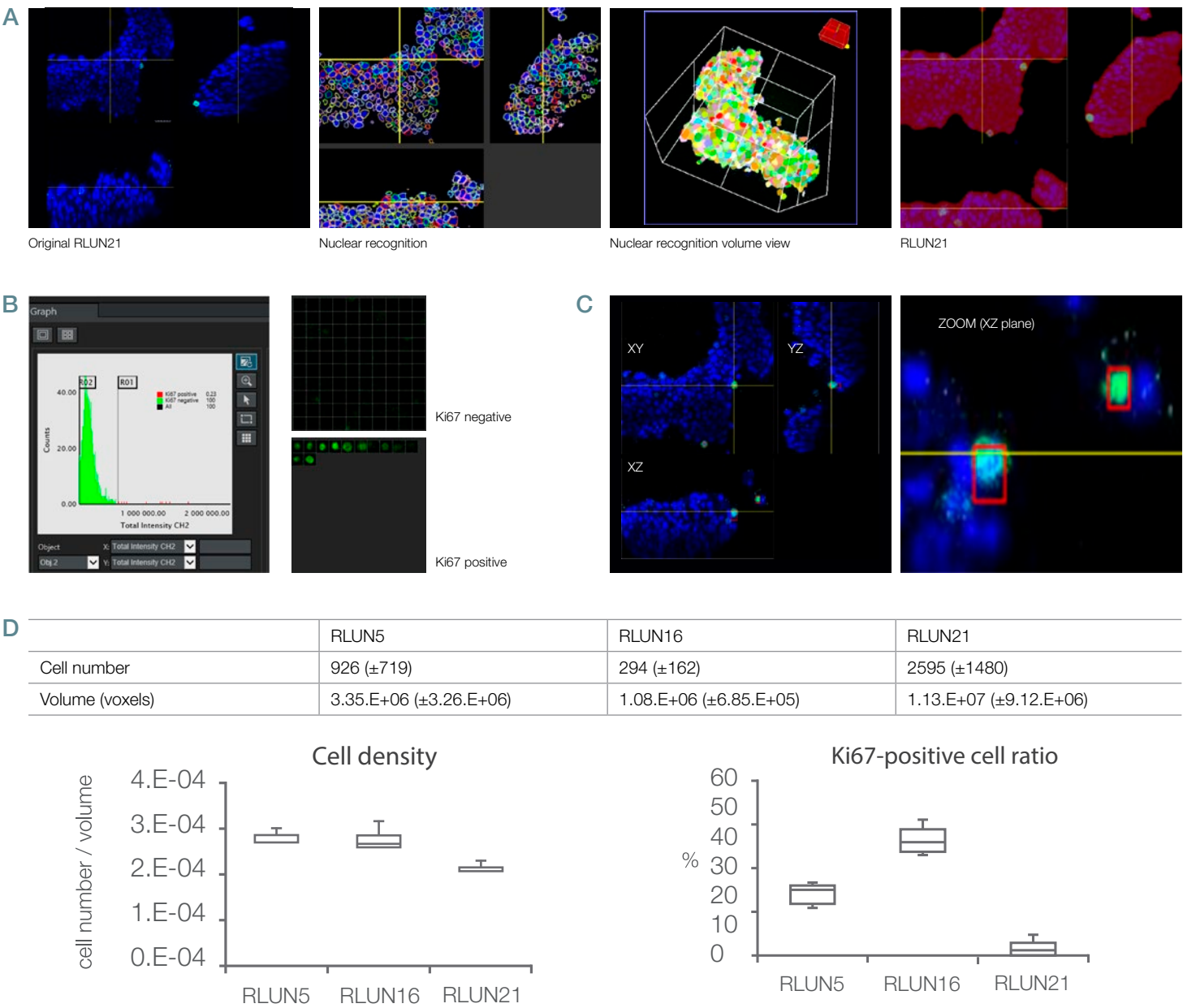


Figure 3. 3D quantification of F-PDOs morphology

A. Original 3-side views of RLUN21, NoviSight 3D nuclear recognition (3-sides and volume view) and NoviSight structure recognition.

B. Ki67 positive/negative cells were sorted by Ki67 intensity. NoviSight software can display sorted cells in a “Gallery view.”

C. Classified Ki67 positive cells can be displayed in 3D with a red outline.

D. Quantitative data of F-PDOs.

3D drug distribution analysis

When we added the HyLight-555-labeled Erbitux or Herceptin to each F-PDO, Erbitux uniformly bound RLUN21 from its surface while Herceptin irregularly bound RLUN21. NoviSight™ software’s volume recognition module quantified the antibody-drug-positive volume ratio (Fig. 4A). We then used NoviSight software to quantify the difference in binding styles since it can modify the analysis-targeted region. To do so, we created two targeted regions: a reduced intra-PDO volume region from the surface at a certain percentage and an outline volume region with any width. We then calculated antibody drug intensity within both volumes. We noticed a large quantitative difference between the reduced intra-PDO volume and outline volume in Erbitux-treated RLUN21, while there was a non-significant difference found in Herceptin-treated RLUN21. This means Erbitux strongly bound to the RLUN21 outline region while Herceptin bound to RLUN21 without bias. This method enabled us to quantitatively show antibody drug distribution within a PDO sample population.

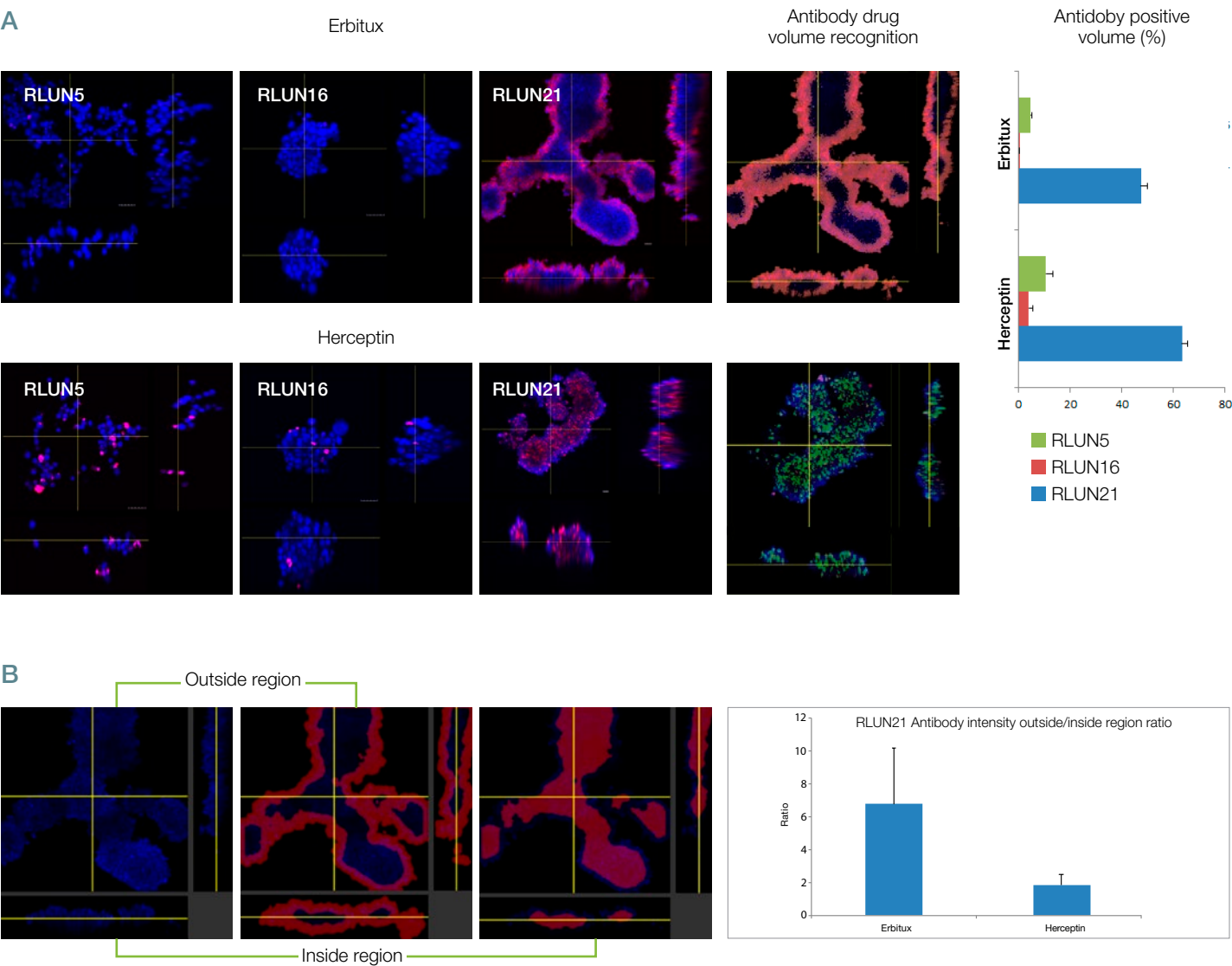


Figure 4. 3D quantification of antibody drug distribution

- A. 3-side images of F-PDOs treated with Erbitux or Herceptin, and NoviSight volume recognition of antibody drug bindings. The graph shows antibody binding volume in whole volume.
- B. NoviSight region modification module. NoviSight software can modify the analysis-targeted region to provide quantitative data in the limited region.

Conclusion

In this study, we revealed that NoviSight software can perform quantitative analysis of PDOs morphologically and pharmacologically using images captured by Olympus' FV3000 confocal laser scanning microscope. By combining the high-resolution images of the FV3000 microscope with the high recognition accuracy of NoviSight software, we can produce more reliable quantitative results.

Reference

1. Vlachogiannis G et al., (2018) Patient-derived organoids model treatment response of metastatic gastrointestinal cancers. *Science*. 359(6378):920–926. doi: 10.1126/science.aao2774
2. Takahashi et al., (2019) An In Vitro System for Evaluating Molecular Targeted Drugs Using Lung Patient-Derived Tumor Organoids. *Cells*. 8(5), 481. doi:/10.3390
3. Tamura H, et al. Evaluation of anticancer agents using patient-derived tumor organoids characteristically similar to source tissues. *Oncol Rep.*,40, 635–646, 2018
4. Hama et al., (2016) Deep Imaging of Cleared Brain by Confocal Laser-Scanning Microscopy. *Nature Protocol Exchange*. doi:/10.1038

Author

Mayu Ogawa (Olympus Corporation)

Acknowledgment

This study was supported by Professor Takagi of Fukushima Medical University.

To learn more about F-PDO (Fukushima patient-derived organoids), please visit <https://www.fmu.ac.jp/home/trc/en/contract-research-provision/f-pdo/>

Evaluation of Drug Efficacy

The Response of Spheroids to a Drug

Confocal observation combined with the use of an FV3000 laser confocal microscope enables the evaluation of drug efficacy in spheroids stained with an appropriate fluorescent dye.

Objectives

The majority of efficacy assays of anticancer drugs have relied on the use of immobilized cells grown as 2D monolayers. However, these 2D monolayers are unable to recapitulate the complex native environment of cancer cells. Therefore, 3D cell cultures such as spheroids are attracting attention as models that have the potential to improve the physiological relevance of cell-based studies. In this study, the efficacy of Staurosporine (STS) in spheroids was evaluated through confocal observation combined with the use of a high-content 3D cell imaging analysis system.

Preparation of samples

A suspension of HeLa cells was seeded into a PrimeSurface® 96U plate (SUMITOMO BAKELITE CO., LTD) at 500 cells/well. Serially-diluted STS was added to each well 48 hours after the start of cell culture. Hoechst 33342 (nuclear staining dye) and propidium iodide (PI: dead cell staining dye) were added to each well 24 hours after the addition of STS.

Conclusion

Acquisition and analysis of fluorescent images

Fluorescent images of the above-mentioned spheroids stained by Hoechst 33342 and PI were obtained using the FV3000 microscope. As shown in Figure 1, the ratio of dead cells (pseudo red) to all cells (pseudo blue) in each well increased with an increase in STS concentration. The ratios can be graphically displayed against STS concentration (Figure 2, bars: SD, n=8), using the nuclei identification and counting results generated by Olympus NoviSight analysis software. These results indicated that the system enables easy evaluation of drug efficacy in one microplate.

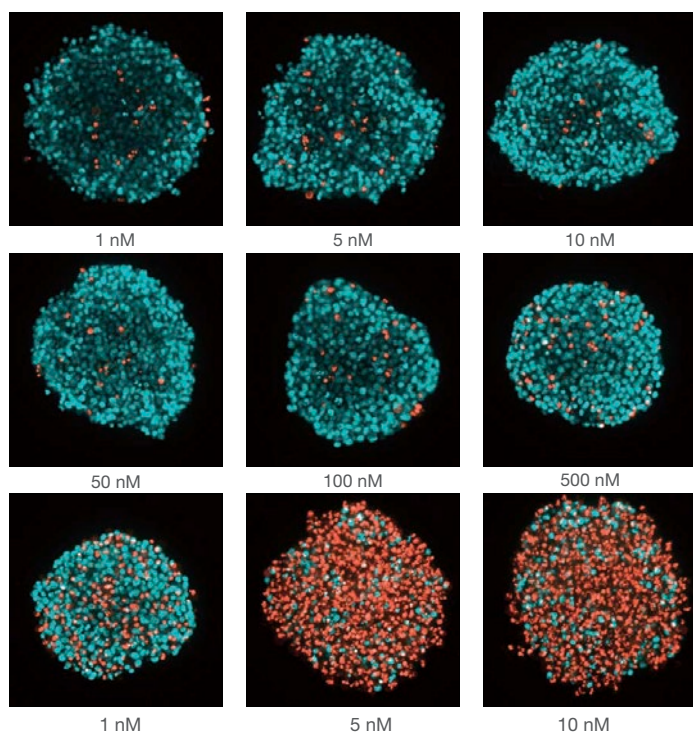


Figure 1. STS concentration-dependent dead cells/all cells images of spheroids

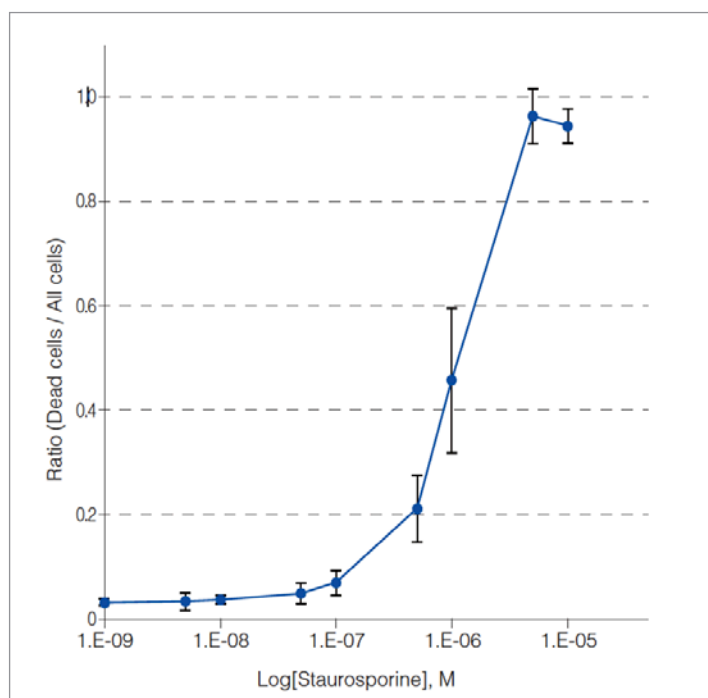


Figure 2. STS concentration-dependent dead cells/all cells ratio in spheroids

Fluorescent Image Analysis

3D Spheroid Invasion in a Collagen Gel

Confocal images of cancer spheroid invasion in a collagen gel were quantitatively evaluated using NoviSight™ software to gauge the impact of an anti-cancer drug that targeted the factor related to tumor invasion.

Objectives

The metastatic cascade can be broadly separated into three main processes: invasion, intravasation, and extravasation. The first step, tumor invasion, is fundamental in tumor progression and is the driving force for metastasis. Tumor invasion is also composed of three processes: degradation of the extracellular matrix (ECM), intercellular adhesion detachment, and cell migration. The ECM is a collection of extracellular molecules, such as collagen, fibronectin, laminin, and proteoglycans, and forms an intricate network. Tumor cells collectively migrate while repeating degradation and reconstruction of the ECM network.

To evaluate invasion capacity or drug efficacy, a wound-healing assay or transwell assay is commonly used. These traditional assays are simple and inexpensive, but they lack the tumor's microenvironment, and the cells lose relevant properties, such as polarization and cell-to-cell communication. Therefore, these artificial assays contribute to the poor predictive value of compound efficacies between in vitro and in vivo experiments. To recreate the tumor microenvironment, a three-dimensional in-gel invasion assay has become a more relevant tool for evaluating anti-cancer drug efficacy. This assay can recreate the tumor microenvironment by embedding tumor spheroids in a gel matrix. The embedded spheroids then gradually sprout into the gel. This assay can closely mimic tumor morphology or the collectiveness of invasion. In this study, NoviSight™ software and a 3D in-gel invasion assay were used to quantitatively analyze the effect of anti-cancer drugs on invasive spheroids. The study demonstrates the software's ability to quantify the invasion of complex-shaped tumors.

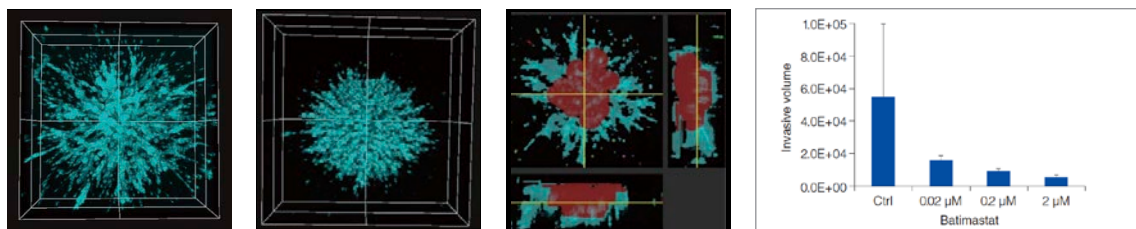
Sample preparation

A cell suspension of human fibrosarcoma cells HT1080 were seeded in a U-bottom 96-well plate (Corning® Inc.) (Day 1). On Day 3, HT1080 spheroids were embedded in matrigel (Corning® Inc.), and a culture medium containing Batimastat, an anticancer drug that specifically inhibits matrix metalloproteinase (MMP), was added over the matrigel. On Day 5, cell nuclei were stained with Hoechst33342.

Conclusion

Acquisition and analysis of fluorescent images

Observations were made using the FV3000 laser confocal microscope. On Day 5, a non-treated spheroid showed powerful invasion (A), however, invasion was inhibited in the presence of Batimastat (B). The invasion area and its complex 3D structure was recognized by NoviSight™ software (C: the red area is the center of a spheroid, and the blue area is the projection portion of invasion). Using the software's volume analysis function, we were able to determine that Batimastat inhibited HT1080 spheroid invasion in a dose-dependent manner (D).



True 3D Analysis of an Intracellular Autophagic Pathway in a 3D Spheroid Model

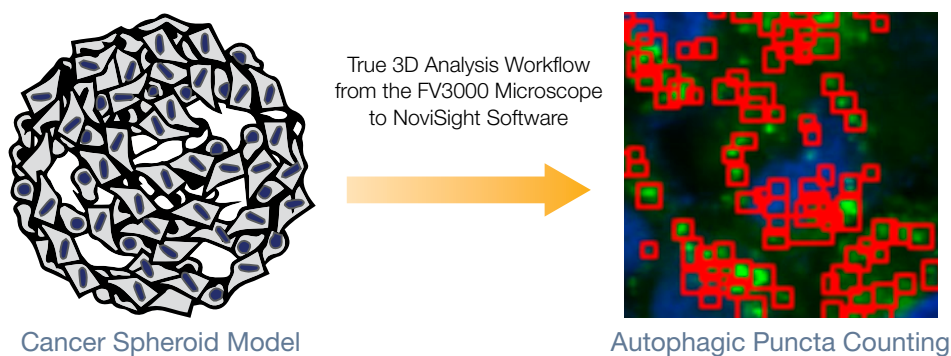
Summary

3D culture models have been used for predicting drug efficacy or toxicity. In this application note, we focus on an intracellular autophagic pathway. First, we confirmed the usefulness of the EGFP-LC3 probe for monitoring the models' autophagic status. Then, Olympus' true 3D analysis workflow using the FLUOVIEW™ FV3000 confocal microscope and NoviSight™ software was used to quantitatively evaluate the effect of a drug candidate called chloroquine. We demonstrated that this analysis workflow offers an alternative to profiling drug candidates using in vivo studies.

Introduction

Intracellular molecular events are closely related to a wide variety of pathologies in humans. Autophagy is an intracellular process that degrades and recycles cellular organelles and proteins, and the dysregulation of autophagy is implicated in human diseases. To better understand these disease processes and test the efficacy of drugs on them, it is important to monitor the autophagic status of human cells under pathological and therapeutic conditions.

3D culture models such as spheroids or organoids closely resemble the complex in vivo microenvironment. To evaluate the efficacy of a drug on the cells in the spheroid, it is critical to quantitatively analyze intracellular microscopic images. In this application note, we assessed a dynamic intramolecular autophagy process and quantitatively evaluated the effect of a drug candidate using the Olympus FV3000 confocal microscope and NoviSight analysis software's true 3D analysis workflow.



Benefits

- Quantitative analysis of intramolecular events in 3D culture models

Results and Discussion

The LC3 protein is a useful marker in an autophagy process. For example, it has been reported that EGFP-LC3 fluorescence dots increased when autophagosomes were accumulated. Autophagosome formation is regulated by various compounds that modulate the autophagic activities or the turnover of autophagosomes. Some of these compounds are now in clinical trials. One, chloroquine (CQ), originally an anti-malarial drug, is now in a clinical trial for cancer treatment because it inhibits the fusion of autophagosomes and lysosomes.

Validation of an autophagy marker using a 2D culture system

We validated the usefulness of an EGFP-LC3 probe to measure the CQ's inhibitory effect on the autophagic process in a 2D culture system. We prepared a U2OS osteosarcoma cell line stably expressing EGFP-LC3. The cells were cultured as monolayers in microplate wells. After adding CQ, the cells were fixed and stained with Hoechst 33342. Fluorescence images showed that CQ treatment evoked the formation of EGFP-LC3 puncta (Figure 1 A and B). The puncta area per cell was measured based on the position of each cell's nucleus. The puncta area increased as the concentration of CQ increased, confirming the usefulness of the EGFP-LC3 probe to measure an autophagic process.

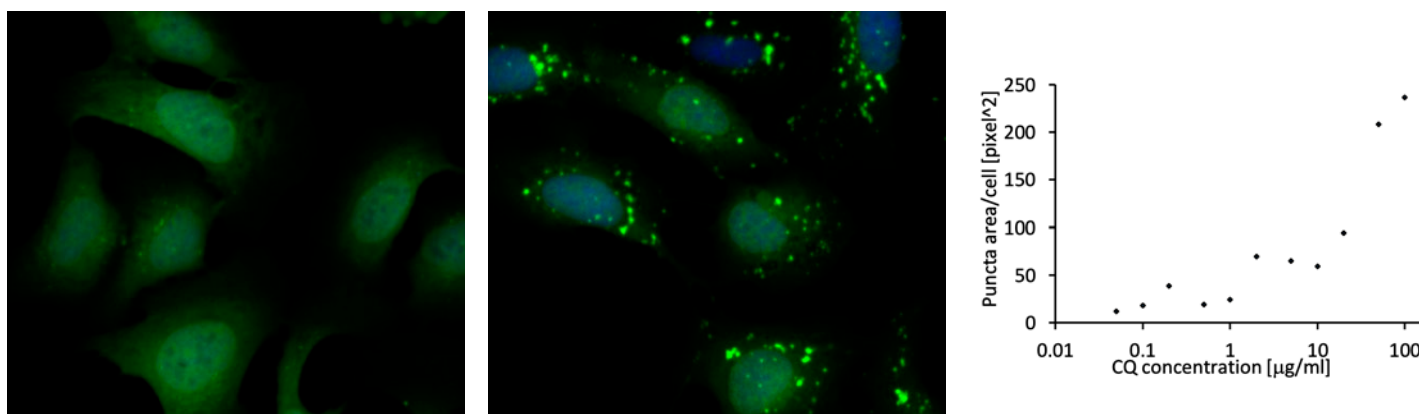


Figure 1 A and 1 B. (A) EGFP-LC3-expressing U2OS cells cultured in normal condition. (B) EGFP-LC3-expressing U2OS cells treated with CQ for one hour. Figure 1 C. The increase of the puncta area per cell plotted with the increase of CQ concentration.

Quantification of LC3 punctate in the cancer spheroid model

To monitor autophagic status in 3D culture models, we selected a HeLa cell line established from cervical carcinoma. The HeLa cells are suited for a scaffold-free 3D culture protocol and form cancer spheroids of uniform size. We prepared a HeLa cell line stably expressing EGFP-LC3.

The cells were seeded in round-bottom, low-attachment microplates. After five days' culture, the spheroids were treated with CQ for seven hours. Then, the spheroids were fixed, membrane-permeabilized, their nuclei stained, and finally cleared with SCALEVIEW-S4 (FUJIFILM WAKO).

We observed the spheroids using Olympus' FLUOVIEW™ FV3000 confocal system. We used a silicone immersion objective (UPLSAPO30XSIR) because of its high numerical aperture (NA) and reduced spherical aberration. Figure 2 (A) shows a single Z-slice image of the non-treated spheroid at the equator. The EGFP signal appeared uniformly in the cells. In contrast, CQ treatment induced the formation of puncta EGFP signals in the cells (Figure 2 (B)). The puncta formations were observed both in the peripheral zone and in the central zone of the spheroid. CQ treatment did not cause any apparent change of the spheroid's size, indicating that the intracellular autophagic process might be a better marker for evaluating the efficacy of CQ in 3D cancer spheroids.

To quantitatively analyze the intracellular events in the 3D culture models, we used Olympus' true 3D analysis workflow that combines images captured using the FV3000 confocal microscope and analysis using NoviSight™ software, which offers many benefits over conventional analytical methods. In a conventional analysis, we would use the integrated characteristic value of the recognized objects from multiple Z-slice images or analyze the projection image of multiple Z-slice images. These methods are unreliable because they can lead to counting objects of interest multiple times or missing objects of interest that were overlapped and obscured by other objects. In contrast, the Olympus true 3D analysis workflow includes the acquisition of sequential Z-slice images with Z-intervals optimized by the FLUOVIEW™ software. The software reconstructed the 3D volume and recognized the objects of interest as clusters of voxels. NoviSight software is then used for statistical analysis. The workflow from FLUOVIEW to NoviSight software is straightforward and offers an ideal platform for the analysis of 3D culture models.

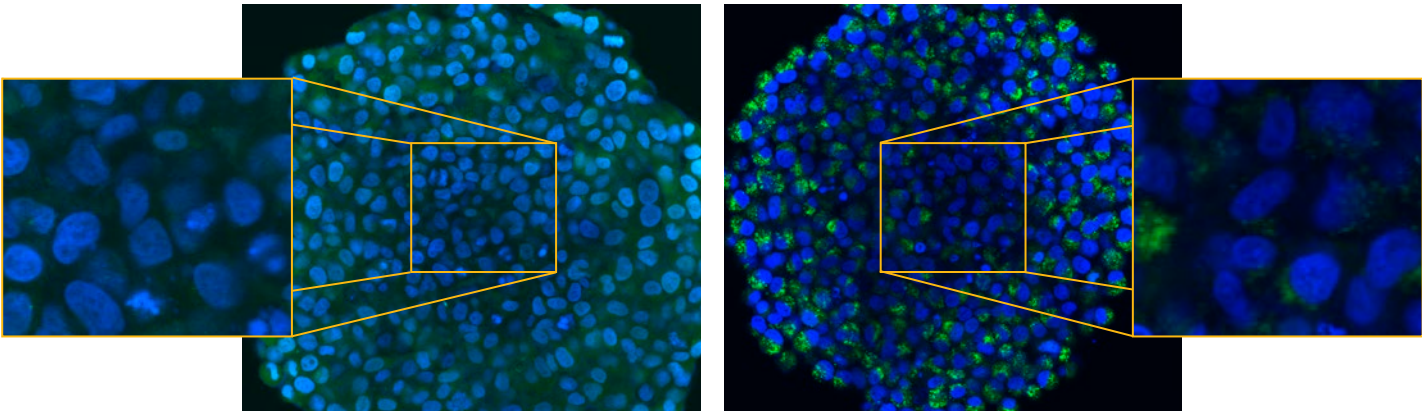


Figure 2 A and 2 B. EGFP-LC3-expressing HeLa cell spheroids (A) in normal condition and (B) treated with CQ. The enlarged images show the yellow rectangle region of the original spheroid images.

To calculate the number of autophagy-positive cells in the spheroid, the software identified the nucleus of each cell. Next, the regions surrounding each nucleus were defined as mask regions. Finally, the puncta of EGFP signals in the mask regions were recognized as puncta objects (Figure 2 (C)). Cells that have more than three puncta were regarded as autophagy-positive cells. The 3D spheroid without drug treatment had about 1.4% autophagy-positive cells, while the spheroid treated with CQ showed 66.6% autophagy-positive cells (Figure 2 (D)). Quantitative analysis also supports that CQ induced the puncta to form in the cancer spheroids.

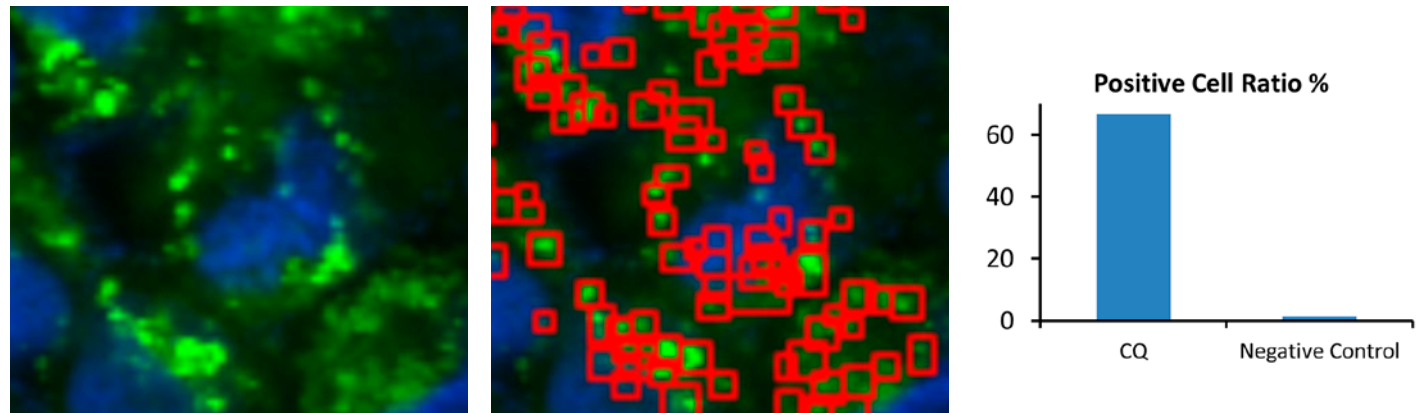


Figure 2 C Left. The original image of the cells in the spheroid with CQ. Right. The same image with object recognition for puncta (red rectangles).
Figure 2 D. The ratio of the cell number to a control showing that it has a higher number of puncta objects than the threshold.

Conclusion

The Olympus FLUOVIEW FV3000 confocal microscope and NoviSight software, as part of a true 3D analysis workflow, were used to quantitatively evaluate the effect of CQ on the intracellular autophagy process in 3D culture models. This study demonstrates that researchers can use this workflow to profile drug efficacy in a dose-dependent manner or screen multiple drug candidates objectively. There are other intracellular molecular markers that are relevant to drug efficacy or drug toxicity, such as FISH signals on chromosomes or translocation of fluorescent-labeled signaling molecules. This workflow can help to quantitatively evaluate a wide range of intracellular events in 3D culture models and offers alternative profiling of drug candidates in lieu of in vivo studies.

References

1. Maria C et al., (2019) Targeting autophagy to overcome human disease. *International Journal of Molecular Sciences*. 20(3): E725. doi: 10.3390/ijms20030725
2. Yan C et al., (2013) Therapeutic targeting of autophagy in disease: Biology and Pharmacology. *Pharmacological Reviews*. 65: 1162–1197. doi: 10.1124/pr.112.007120
3. Daniel JK et al., (2008) Guidelines for the use and interpretation of assays for monitoring autophagy in higher eukaryotes. *Autophagy*. 4(2): 151–175. doi: 10.4161/auto.5338

Author

Kazuhito Goda (Olympus Corporation)

- OLYMPUS CORPORATION is ISO14001 certified.
- OLYMPUS CORPORATION is ISO9001 certified.
- Illumination devices for microscope have suggested lifetimes. Periodic inspections are required. Please visit our website for details.
- All company and product names are registered trademarks and/or trademarks of their respective owners.
- Olympus, the Olympus logo, FLUOVIEW, and NoviSight are trademarks of Olympus Corporation or its subsidiaries.
- Images on the PC monitors are simulated.
- Specifications and appearances are subject to change without any notice or obligation on the part of the manufacturer.

www.olympus-lifescience.com

OLYMPUS

OLYMPUS CORPORATION
Shinjuku Monolith, 2-3-1 Nishi-Shinjuku, Shinjuku-ku, Tokyo 163-0914, Japan